國立臺灣大學理學院化學所

碩士論文

Department of Chemistry

College of Science

National Taiwan University

Master's Thesis

統一福斯特以及修正瑞德菲爾動力學的新理論: 純相移變分極化子參考系統量子主方程

Unified Theory for Förster and Redfield Dynamics: a Pure Dephasing Variational Polaron Reference System Quantum Master Equation

黃品澤

Pin-Tse Huang

指導教授: 鄭原忠 博士

Advisor: Yuan-Chung Cheng Ph.D.

中華民國 113 年 9 月

September, 2024

doi:10.6342/NTU202404389

Acknowledgements

感謝鄭老師的指導，在碩士的路途中讓我獲益良多，以及金老師在每次 group meeting 給出的意見，讓我能獲得多元及專業的反饋。感謝實驗室的同學每一次的討論，以及所有幫助過我的人。

doi:10.6342/NTU202404389

doi:10.6342/NTU202404389

摘要

激發能量轉移在光合作用系統中發揮關鍵作用。這個過程的效率和根本重要性使激發能量轉移研究成為科學探究的一個重要領域。激發能量轉移動力學建模的傳統方法，例如用於非相干能量轉移的福斯特理論 (FT) 和用於相干轉移的修正雷德菲爾德理論 (CMRT)，在各種系統中都面臨著限制。本研究引入了一個統一的量子主方程式框架，稱為純相移變分極化子參考系統量子主方程式（PDVPRS-QME），它融合了 FT 和 CMRT 的特點，彌補了這些傳統範式之間的差距。PDVPRS-QME 考慮了獨特的交叉項，這對於準確捕捉中間狀態的動態至關重要，同時提供跨不同系統浴耦合強度的更廣泛的適用性。透過針對準絕熱傳播器路徑積分結果的數值基準以及與 FT 和 CMRT 的比較，PDVPRS-QME 被證明可以透過確定最佳參考系統來改進傳統的微擾方法。這項研究強調了選擇適當基礎的重要性，並為推導量子主方程式提供了新的視角。

關鍵字：激發能傳遞、量子主方程式

doi:10.6342/NTU202404389

doi:10.6342/NTU202404389

Abstract

Excitation energy transfer (EET) plays a pivotal role within photosynthetic systems. The efficiency and fundamental importance of this process elevate the study of EET as a vital area of scientific inquiry. Traditional methodologies for modeling EET dynamics, such as Förster Theory (FT) for incoherent energy transfer and the modified Redfield Theory (mRT) for coherent transfer, face limitations across various parameter regimes. This study introduces a unified quantum master equation framework, referred to as pure dephasing variational polaron reference system quantum master equation (PDVPRS-QME), which melds the characteristics of both FT and CMRT to bridge the gap between these traditional paradigms. The PDVPRS-QME accounts for unique cross-terms essential for accurately capturing the dynamics in intermediate system-bath coupling regimes alongside providing broader applicability across a broad range of system-bath coupling strengths. Through numerical benchmarks against quasiadiabatic propagator path integral (QUAPI) results and comparison with FT and CMRT, PDVPRS-QME is demonstrated to improve

doi:10.6342/NTU202404389

upon conventional perturbative approaches by determining an optimal reference system. This study underscores the significance of selecting an appropriate basis and provides a novel perspective for deriving QME.

Keywords: Excitation energy transfer, Quantum master equation

doi:10.6342/NTU202404389

Contents

doi:10.6342/NTU202404389

doi:10.6342/NTU202404389

doi:10.6342/NTU202404389

doi:10.6342/NTU202404389

List of Figures

doi:10.6342/NTU202404389

doi:10.6342/NTU202404389

doi:10.6342/NTU202404389

doi:10.6342/NTU202404389

Denotation

QME	Quantum Master Equation
FT	Förster Theory
RT	Redfield Theory
mRT	Modified Redfield Theory
CMRT	Coherent Modified Redfield Theory
PDRS	Pure Dephasing Reference System
PDVPRS	Pure Dephasing Variational Polaron Reference System
PDVPRS-QME	Pure Dephasing Variational Polaron Reference System Quantum Master Equation

doi:10.6342/NTU202404389

doi:10.6342/NTU202404389

Chapter 1 Introduction

1.1 Excitation energy transfer in photosynthetic systems

Excitation energy transfer (EET) is a crucial mechanism within photosynthetic systems, where it plays a central role in the process of converting of solar energy into chemical energy. Upon absorption of solar photons, light-harvesting antenna molecules are excited and initiate a chain of energy transfer events. This process involves the sequential relay of energy through a network of light-harvesting pigments, ultimately resulting in its delivery to the reaction center. In addition to its fundamental importance, the EET process also exhibits a particularly high quantum efficiency[1–5]. The remarkable efficiency with which this transfer occurs has profound implications for the understanding of photosynthetic machinery, thereby positioning the detailed study of EET as a vital area of scientific inquiry.

1.2 Conventional Theories

Förster theory (FT)[6] is a conventional perturbative approach to model EET dynamics based on excitonic localized on each individual molecules. From an incoherent picture that neglects quantum coherence between different molecules, FT describes a trans-

doi:10.6342/NTU202404389

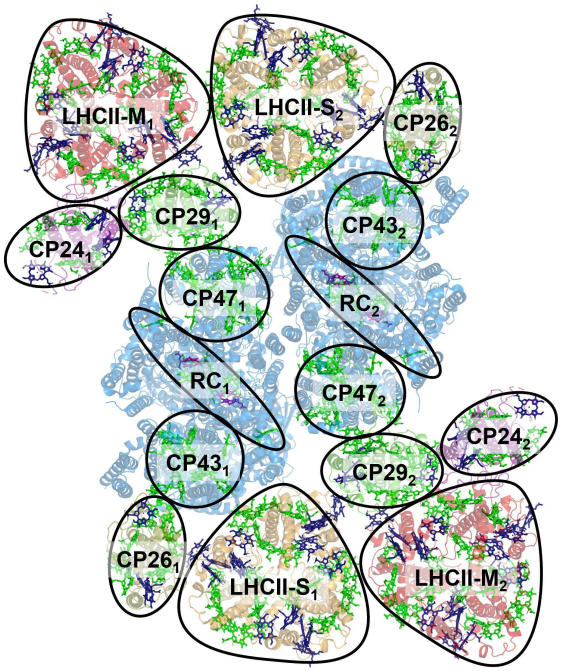

Figure 1.1: Photosystem II (PSII)

fer from donor to acceptor by treating transition dipole-transition dipole interaction as the perturbation. Furthermore, to describe dynamics in a multi-chromophoric system, generalized Förster theory (gFT)[7, 8] was developed. Generalized Förster theory describes a cluster of donors transfer energy to a cluster of acceptors. Dipole interactions between molecules of donor and acceptor are treated as perturbation. However, FT and gFT hold true only when the electronic interactions between the donor and acceptor are significantly less intense compared to the system-bath couplings.

On the other hand, Redfield theory (RT) has long been utilized for studying open quantum system dynamics on the coherent limit for problems such as nuclear magnetic resonance. Redfield theory derives from the electronic eigenbasis which will be referred to as exciton basis and treats the whole system-bath couplings as perturbation to obtain the full dynamics of the reduced density matrix of the system. Because the total system-bath couplings in a photosynthetic system is often not a small parameter, RT usually is not an adequate approach for the dynamics of EET on photosynthesis.

doi:10.6342/NTU202404389

Modified Redfield theory (mRT)[9, 10] improves upon traditional Redfield theory by treating only the off-diagonal terms of system-bath couplings in excition basis as perturbation. The perturbation would be valid in a weak system-bath regime and strong system-bath coupling regime with localized system[10, 11]. Therefore, mRT has a broader applicability than FT and RT. However, mRT describes only population transfer in exciton basis by deriving from a conventional Zwanzig-Nakajima projection technique. One can not obtain the density matrix in site basis because lack of the information of coherence.

Therefore, our group has developed a coherent modified Redfield theory (CMRT)[11, 12] which is a non-Markovian time-local quantum master equation deriving by a second order cumulant expansion. CMRT describes the coherent and disspative dynamics in the same form as the Redfield theory. In this approach, the disspative kernel is the same as mRT which induces the population transfer and dephasing. The diagonal terms of system-bath couplings are included in zeroth order Hamiltonian and induces a pure dephasing. More recently, Trushechkin derived formulas for calculating the coherences in FT and mRT by a Zwanzig-Nakajima projection approach.[13] However, when the energy gap is much smaller than the electronic coupling, the CMRT overestimates the transfer rates and the mRT approach by Trushechkin underestimates the dephasing rate. Both failures can be attributed to the improperly over-delocalized basis.

In exploring the complexities of Excitation Energy Transfer (EET), it's clear that methods such as Förster theory (FT) and modified Redfield theory (mRT) have their limitations. Each has its strengths, yet neither provides a comprehensive solution for the vast array of EET scenarios. However, in real systems, such as photosystem II (PSII) shown in Fig. 1.1, the electronic couplings are typically around 50 cm^{-1} , while the energy gaps can vary widely, ranging from a few hundred cm^{-1}down to just a few cm^{-1}. This wide

doi:10.6342/NTU202404389

range of energy gaps creates a challenge for traditional models, as the dynamics cannot be fully captured by either a purely localized or purely delocalized basis.

Due to the repetitive failures of generalized Förster theory (gFT) and modified Redfield theory (mRT) in accurately modeling Excitation Energy Transfer (EET) dynamics, Novoderezhkin et al. proposed a combined modified Redfield-generalized Förster approach[14–16]. This method adapts to different regimes by calculating transfer rates using mRT or CMRT when electronic couplings exceed a certain cut-off value, and by using gFT when the couplings are below this threshold.

This hybrid approach has demonstrated good performance and has become the standard method in the study of photosynthetic light harvesting[14–18]. However, the effectiveness of this method heavily relies on the choice of an artificial cut-off coupling, which can introduce uncertainties. Additionally, this approach still struggles to accurately describe intermediate cases that lie between the mRT and FT regimes, where neither method alone is entirely adequate[16]. These limitations highlight the ongoing need for more flexible and universally applicable frameworks in EET dynamics research.

1.3 Pure-Dephasing Reference System Approach

Acknowledging the pressing need for a method that adapts across the full spectrum of interaction strengths and coupling regimes, we turn our attention to pure dephasing reference system (PDRS)[19, 20] and small polaron[21–25] approaches. The mRT is a form of PDRS-QME which chooses the electronic eigenstate as the reference system. The PDRS tackles pure dephasing by including diagonal system-bath couplings in the reference Hamiltonian. Moreover, because the pure dephasing effect converges hardly [26],

doi:10.6342/NTU202404389

PDRS approach treats the diagonal system-bath coupling which induced the pure dephasing to all orders instead of second orders.

The small polaron framework handles strong system-bath couplings by folding the influence of the environment into an effective system Hamiltonian. Therefore, the small polaron approach describes the dynamical localization effect well. Unlike Redfield theory, which performs well in the weak coupling regime, the small polaron quantum master equation excels in the strong coupling regime[23], offering a complementary approach to capture the dynamics where RT and CMRT may fail.

1.4 Content in This Work

Building on these insights, we have developed a pure dephasing variational polaron reference system quantum master equation (PDVPRS-QME). This novel equation diverges from conventional FT and CMRT frameworks by not requiring the basis in the PDRS to be entirely localized or delocalized. To identify the optimal basis within the PDRS, we employ the variational polaron approach, allowing us to determine an optimal reference system through Bogoliubov's theorem. Furthermore, the population transfer rate in PDVPRS-QME comprises a combination of mRT, FT, and a unique cross term. The cross term becomes particularly significant when the PDVPRS operates in an intermediate regime. After benchmarking against conventional methods and the gold-standard approach, PDVPRS-QME demonstrates broader applicability across various regimes, effectively circumventing the limitations of traditional theories.

doi:10.6342/NTU202404389

doi:10.6342/NTU202404389

Chapter 2 Generalized Pure Dephasing Reference System Quantum Mater Equation

2.1 Model Dimer System

2.1.1 Frenkel Exciton Hamiltonian

We start from a generic system-bath Hamiltonian for a dimer system in the site basis,where the total Hamiltonian is

$$H = H_s + H_b + H_{sb}, \tag{2.1}$$

and the system part is

$$H_s = \Delta(|D\rangle\langle D| - |A\rangle\langle A|) + J_0(|D\rangle\langle A| + |A\rangle\langle D|), \tag{2.2}$$

doi:10.6342/NTU202404389

with $|D\rangle$ and $|A\rangle$ representing electronic states localized at donor and acceptor, respectively. 2Δ is the energy gap between $|D\rangle$ and $|A\rangle$, and J_0 is the electonic coupling. Furthermore, the bath part is described by a set of harmonic oscillators, where the bath Hamiltonian is

$$H_b = \sum_{n=D,A} \sum_i \omega_{ni} b_{ni}^\dagger b_{ni}, \tag{2.3}$$

with $b_{ni}(b_{ni}^\dagger)$ is the annihilation(creation) operator of the i-th vibrational mode on site n, and ω_{ni} is the vibrational energy of the mode. For system-bath coupling, we consider a site-diagonal bilinear system-bath coupling:

$$H_{sb} = \sum_{n=D,A} \sum_i g_{ni}\omega_{ni}(b_{ni}^\dagger + b_{ni})|n\rangle\langle n|, \tag{2.4}$$

where g_{ni} is a dimensionless electron-phonon coupling strength constant. Note that we set $\overline{h} = \frac{h}{2\pi} = 1$, where h is the Planck constant.

2.1.2 Electronic Reference System

Diverging from traditional CMRT or FT, we start from an arbitrary electronic reference system defined by a mixing angle θ. Therefore, we perform an unitary transformation U on the total Hamiltonian to convert it into an arbitrary basis,

$$\widetilde{H} = U^\dagger H U = \widetilde{H}_s + \widetilde{H}_b + \widetilde{H}_{sb}, \tag{2.5}$$

doi:10.6342/NTU202404389

and for a dimer system, an unitary transformation is a rotation operator:

$$U = \begin{bmatrix} cos(\theta) & -sin(\theta) \\ sin(\theta) & cos(\theta) \end{bmatrix}. \tag{2.6}$$

The system part becomes

$$\widetilde{H}_s = \widetilde{\Delta}(|\alpha\rangle\langle\alpha| - |\beta\rangle\langle\beta|) + \widetilde{J}(|\alpha\rangle\langle\beta| + |\beta\rangle\langle\alpha|), \tag{2.7}$$

where $|\alpha\rangle = C_D^\alpha|D\rangle + C_A^\alpha|A\rangle$, is a linear combination of $|1\rangle$ and $|2\rangle$,and $\widetilde{\Delta}$ and $\widetilde{J}$ describe the energy gap and electronic coupling between $|\alpha\rangle$ and $|\beta\rangle$. Moreover, the bath Hamiltonian has not changed after the transformation, i.e. $\widetilde{H}_b = H_b$. Subsequently, the system-bath coupling becomes

$$\widetilde{H}_{sb} = \sum_{\alpha,\beta}\sum_{n=D,A}\sum_i C_n^\alpha C_n^{\beta*} g_{ni}\omega_{ni}(b_{ni}^\dagger + b_{ni})|\alpha\rangle\langle\beta|, \tag{2.8}$$

$$= H_{sb}^{\alpha\alpha}|\alpha\rangle\langle\alpha| + H_{sb}^{\beta\beta}|\beta\rangle\langle\beta| + H_{sb}^{\alpha\beta}|\alpha\rangle\langle\beta| + H_{sb}^{\beta\alpha}|\beta\rangle\langle\alpha|, \tag{2.9}$$

where $H_{sb}^{\alpha\beta} = \langle\alpha|H_{sb}|\beta\rangle$.

2.1.3 Zeroth Order Hamiltonian and Perturbation

To derive a quantum master equation, we partition the total Hamiltonian into zeroth-order Hamiltonian (H_0) and perturbation Hamiltonian (V). Here we treat all off-diagonal

doi:10.6342/NTU202404389

terms in the electronic reference system as perturbation,

$$V = \widetilde{H}_{s,off} + \widetilde{H}_{sb,off}, \tag{2.10}$$

$$\widetilde{H}_{s,off} = \widetilde{J}(|\alpha\rangle\langle\beta| + |\beta\rangle\langle\alpha|), \tag{2.11}$$

$$\widetilde{H}_{sb,off} = H_{sb}^{\alpha\beta}|\alpha\rangle\langle\beta| + H_{sb}^{\beta\alpha}|\beta\rangle\langle\alpha|, \tag{2.12}$$

and zeroth-order Hamiltonian is

$$H_0 = \widetilde{H}_{s,diag} + \widetilde{H}_b + \widetilde{H}_{sb,diag}, \tag{2.13}$$

$$\widetilde{H}_{s,diag} = \widetilde{\Delta}(|\alpha\rangle\langle\alpha| - |\beta\rangle\langle\beta|), \tag{2.14}$$

$$\widetilde{H}_{sb,diag} = H_{sb}^{\alpha\alpha}|\alpha\rangle\langle\alpha| + H_{sb}^{\beta\beta}|\beta\rangle\langle\beta|. \tag{2.15}$$

As the mixing angle varies from 0 to its maximum value, the selection of the reference system changes from the FT picture (site basis) to the CMRT picture (exciton basis, i.e. electronic eigenstate). Additionally, the perturbation changes from electronic coupling to the off-diagonal terms of the system-bath coupling. Intermediately, the reference system between the two pictures gives rise to a mix perturbation that includes both.

2.2 Generalized PDRS Quantum Master Equation

2.2.1 General Time Local Quantum Master Equation

To obtain the equation of motion of population and coherence, we start from the Liouville equation in the interaction picture:

$$\dot{\rho}_I(t) = -i[V_I(t), \rho_I(t)], \tag{2.16}$$

doi:10.6342/NTU202404389

where $\rho_I(t) = e^{iH_0 t}\rho(t)e^{-iH_0 t}$ is the density matrix in the interaction picture and $\rho(t)$ is density matrix in the Schrödinger picture and $V_I(t) = e^{iH_0 t}V_I e^{-iH_0 t}$ is the perturbation in the interaction picture. Utilizing the second order cumulant expansion with respect to V, we obtain

$$\dot{\sigma_I}(t) = \int_0^t \mathrm{Tr}_B \left\{ [V_I(t), [V_I(\tau), \sigma(t) \otimes \rho_{eq}^b]] \right\} d\tau, \tag{2.17}$$

where $\sigma_I(t)$ is the system density matrix in the interaction picture and ρ_b^{eq} is the equilibrium density matrix of the bath.

In Schrödinger picture, the system density matrix is $\sigma(t) = \mathrm{Tr}_B\{U_0\sigma_I(t)\rho_b^{eq}U_0^\dagger\}$. Therefore, the equation of motion of reduced density matrix in the Schrödinger picture is

$$\begin{aligned}\dot{\sigma}(t) &= -i\mathrm{Tr}_B \left\{ [H_0, \sigma(t) \otimes \rho_{eq}^b] \right\} - \int_0^t \mathrm{Tr}_B \left\{ [V, [V(-\tau), \sigma(t) \otimes \rho_{eq}^b]] \right\} d\tau \\ &= \dot{\sigma}^{(\mathrm{coh})}(t) + \dot{\sigma}^{(\mathrm{diss})}(t),\end{aligned} \tag{2.18}$$

The former part of equation describes the coherent dynamics and the latter part describes the dissipative dynamics.

2.2.2 Coherent Part of QME

First, for the coherent part, we consider the density matrix $\sigma(t)$ is driven by the H_0 which can be exactly evaluated:

$$\sigma^{\mathrm{coh}}(t) = \mathrm{Tr}_B\{U_0(t)\sigma(0)U_0^\dagger(t)\}. \tag{2.19}$$

doi:10.6342/NTU202404389

For the element of density matrix $\sigma_{\alpha\beta}(t) = \langle\alpha|\sigma(t)|\beta\rangle$, we can obtain

$$\sigma^{\text{coh}}_{\alpha\beta}(t) = e^{-i(\epsilon_\alpha-\epsilon_\beta)t}\text{Tr}_B\{e^{-i(H_{ph}+H^{\alpha\alpha}_{sb})t}\rho^b_{eq}e^{i(H_{ph}+H^{\beta\beta}_{sb})t}\sigma_{\alpha\beta}(0)\}, \tag{2.20}$$

where ϵ_α and ϵ_β are the site energy of $|\alpha\rangle$ and $|\beta\rangle$. The former term describes the coherent evolution of system and the latter term contributes a pure dephasing of coherence which can be evaluated by thermal average. Note that the coherent part do not contribute to the dynamics of population because $\epsilon_\alpha - \epsilon_\beta = 0$.

Finally, after taking the derivative in time, the coherent dynamics consists of a coherent evolution which driven by the system Hamiltonian and a pure dephasing of coherence induced by the diagonal terms of $\widetilde{H}_{sb}$:

$$\dot{\sigma}^{(\text{coh})}_{\alpha\beta}(t) = -i(2\widetilde{\Delta})\sigma_{\alpha\beta}(t) - R^{pd}_{\alpha\beta}(t)\sigma_{\alpha\beta}(t), \tag{2.21}$$

where the pure dephasing rate[12] is

$$\begin{aligned} R^{\text{pd}}_{\alpha\beta}(t) = &\text{Re}[\dot{g}_{\alpha\alpha\alpha\alpha}(t) + \dot{g}_{\beta\beta\beta\beta}(t) - 2\dot{g}_{\alpha\beta\alpha\beta}(t)] \\ &+ i\text{Im}[\dot{g}_{\alpha\alpha\alpha\alpha}(t) - \dot{g}_{\beta\beta\beta\beta}(t)], \end{aligned} \tag{2.22}$$

with $g_{\alpha\beta\gamma\delta}(t)$ is the lineshape function:

$$\begin{aligned} g_{\alpha\beta\gamma\delta}(t) = &\sum_{n,m} c^\alpha_n c^{\beta*}_n c^\gamma_m c^{\delta*}_m \\ &\int_0^\infty d\omega \frac{J_{nm}(\omega)}{\omega^2}\left\{\left[\coth\left(\frac{\omega}{2k_BT}\right)(1-\cos(\omega t))\right]\right. \\ &\left.+ i\Big[\sin(\omega t) - \omega t\Big]\right\} = \sum_{n,m} c^\alpha_n c^{\beta*}_n c^\gamma_m c^{\delta*}_m g_{nm}(t), \end{aligned} \tag{2.23}$$

where J_{nm} is a spectral density representing the coupling-weighted density of state used to

doi:10.6342/NTU202404389

describe the complicated interaction between bath and system in condensed phase system:

$$J_{nm}(\omega) = \sum_i g_{ni} g_{mi} \omega_i^2 \delta(\omega - \omega_i). \tag{2.24}$$

In the following discussion, we apply a site-independent baths and site-diagonal system-bath coupling by a super-ohmic spectral density: $J_{DD}(\omega) = J_{AA}(\omega) = \gamma\omega^3 e^{-\omega/\omega_c}/\pi\omega_c^2$ where γ is system-bath coupling constant and ω_c is the cut-off frequency.

2.2.3 Incoherent Part of QME

Next, the dissipation part of dynamics is following:

$$\dot{\sigma}^{(\text{diss})}(t) = -\int_0^t d\tau \text{Tr}_B \left\{ [V, [V(-\tau), \sigma(t) \otimes \rho_{eq}^b]] \right\}, \tag{2.25}$$

and evaluated to yield this equation of motion,

$$\dot{\sigma}_{\alpha\beta}^{(\text{diss})}(t) = \sum_{\gamma\delta} \left(\Gamma_{\delta\beta,\alpha\gamma} + \Gamma_{\gamma\alpha,\beta\delta}^* - \delta_{\beta\delta} \sum_f \Gamma_{\alpha f,f\gamma} - \delta_{\alpha\gamma} \sum_f \Gamma_{\beta f,f\delta}^* \right) \sigma_{\gamma\delta}(t), \tag{2.26}$$

where $\Gamma_{\alpha\beta,\gamma\delta} = \int_0^t d\tau \langle V_{\alpha\beta} V_{\gamma\delta}(-\tau) \rangle$, and $\langle \cdot \rangle$ represents the thermal average with $V_{\alpha\beta}(-\tau) = \langle \alpha | V(-\tau) | \beta \rangle$.

For $\alpha = \beta$ and $\gamma = \delta$, the equation 2.26 produces the population transfer dynamics:

$$\dot{\sigma}_{\alpha\alpha}^{(\text{diss})}(t) = \sum_\gamma \left(R_{\alpha\gamma} \sigma_{\gamma\gamma}(t) - R_{\gamma\alpha} \sigma_{\alpha\alpha}(t) \right), \tag{2.27}$$

where the transfer rate from $|\beta\rangle$ to $|\alpha\rangle$ is

$$R_{\alpha\beta}(t) = 2 \cdot \text{Re} \int_0^t d\tau \langle V_{\beta\alpha} V_{\alpha\beta}(-\tau) \rangle. \tag{2.28}$$

doi:10.6342/NTU202404389

The dephasing of electronic coherence induced by perturbation is corresponding to $\alpha \neq \beta, \gamma = \alpha, \delta = \beta$. After evaluated the dephasing rate is composed of the average of population transfer rate between dimer and imaginary part of the time correlation function of perturbation:

$$\dot{\sigma}^{(\text{diss})}_{\alpha\beta}(t) = -\left[\frac{1}{2}\left(R_{\beta\alpha} + R_{\alpha\beta}\right) + i \cdot \text{Im}\left(\Gamma_{\alpha\beta,\beta\alpha} + \Gamma^{*}_{\beta\alpha,\alpha\beta}\right)\right]\sigma_{\alpha\beta}(t). \tag{2.29}$$

In our calculation, we ignore the imaginary part for simplification because of its tiny effect.

2.2.4 Intrinsically Secular Form

Apart from the secular terms which describe population transfer and dephasing, the non-secular terms representing population-coherence transfer and coherence-coherence transfer are included in the full tensor. Eq.2.26 produces the dynamics which describes population transfer to coherence for $\alpha = \beta, \gamma \neq \delta$

$$\begin{aligned}\dot{\sigma}_{\alpha\alpha}(t) =& (\Gamma_{\beta\alpha,\alpha\alpha} + \Gamma^{*}_{\alpha\alpha,\alpha\beta} - \Gamma^{*}_{\alpha\alpha,\alpha\beta} - \Gamma^{*}_{\alpha\beta,\beta\beta})\sigma_{\alpha\beta}(t) \\ & (\Gamma_{\alpha\alpha,\alpha\beta} + \Gamma^{*}_{\beta\alpha,\alpha\alpha} - \Gamma_{\alpha\alpha,\alpha\beta} - \Gamma_{\alpha\beta,\beta\beta})\sigma_{\beta\alpha}(t),\end{aligned} \tag{2.30}$$

and $\alpha \neq \beta, \gamma = \delta$ for coherence transfer to population

$$\begin{aligned}\dot{\sigma}_{\alpha\beta}(t) =& (\Gamma_{\alpha\beta,\alpha\alpha} + \Gamma^{*}_{\alpha\alpha,\beta\alpha} - \Gamma^{*}_{\beta\alpha,\alpha\alpha} - \Gamma^{*}_{\beta\beta,\beta\alpha})\sigma_{\alpha\alpha}(t) \\ & (\Gamma_{\beta\beta,\alpha\beta} + \Gamma^{*}_{\beta\alpha,\beta\beta} - \Gamma_{\alpha\alpha,\alpha\beta} - \Gamma_{\alpha\beta,\beta\beta})\sigma_{\beta\beta}(t).\end{aligned} \tag{2.31}$$

However, for population-coherence transfer, all transfer rates involve $V_{\alpha\alpha}$ or $V_{\beta\beta}$ which equal to zero because the perturbation is off-diagonal only. Therefore, a population-coherence transfer does not occur in our theory.

doi:10.6342/NTU202404389

In addition, the dynamics of coherence-coherence transfer yields from $\alpha = \gamma, \beta \neq \delta$

$$\dot{\sigma}_{\alpha\beta}(t) = (\Gamma_{\alpha\beta,\alpha\beta} + \Gamma^*_{\beta\alpha,\beta\alpha})\sigma_{\beta\alpha}(t) \tag{2.32}$$

$$\dot{\sigma}_{\beta\alpha}(t) = (\Gamma_{\beta\alpha,\beta\alpha} + \Gamma^*_{\alpha\beta,\alpha\beta})\sigma_{\alpha\beta}(t). \tag{2.33}$$

The coherence-coherence transfer rates are non-zero but the transfer rates between $\sigma_{\alpha\beta}(t)$ and $\sigma_{\beta\alpha}(t)$ are the same and $\sigma_{\alpha\beta}(0)$ as well as $\sigma_{\beta\alpha}(0)$ are also the same. As a result, a coherence-coherence transfer doesn't exist also.

From the discussion above, our theory is secular naturally for a dimer system. Nevertheless, non-secular terms could play a role in a larger system.

2.2.5 Total Equation of Motion

Finally, the total equation of motion is:

$$\begin{aligned}\dot{\sigma}_{\alpha\beta}(t) = &-i(2\widetilde{\Delta})\sigma_{\alpha\beta}(t) \\ &+ \left[R_{\alpha\beta}(t)\sigma_{\beta\beta}(t) - R_{\beta\alpha}(t)\sigma_{\alpha\alpha}(t)\right]\delta_{\alpha\beta} \\ &- \left[R^{\text{pd}}_{\alpha\beta}(t) + \frac{1}{2}\left(R_{\beta\alpha}(t) + R_{\alpha\beta}(t)\right)\right]\sigma_{\alpha\beta}(t)\,.\end{aligned} \tag{2.34}$$

Up to this point, we have completed the generalized quantum master equation in an arbitrary electronic reference system. Note that CMRT and FT are special cases for the PDVPRS-QME for $\theta = \theta_R$ (mixing angle of eigenstates corresponding to Redfield theory) and $\theta = 0$. In next section, we aim to determine an appropriate basis with a variational approach.

doi:10.6342/NTU202404389

2.3 Population Transfer Rate in the PDRS

Because the perturbation

$$V = \widetilde{H}_{s,off} + \widetilde{H}_{sb,off}, \tag{2.35}$$

has two part, the population transfer rate

$$\begin{aligned} R_{\alpha\beta}(t) &= 2 \cdot \mathrm{Re} \int_0^t d\tau \langle V_{\beta\alpha} V_{\alpha\beta}(-\tau) \rangle \\ &= 2 \cdot \mathrm{Re} \int_0^t d\tau \langle (\widetilde{H}^{\beta\alpha}_{s,off} + \widetilde{H}^{\beta\alpha}_{sb,off})(\widetilde{H}^{\alpha\beta}_{s,off}(-\tau) + \widetilde{H}^{\alpha\beta}_{sb,off}(-\tau)) \rangle \\ &= 2 \cdot \mathrm{Re} \int_0^t d\tau \{ \langle \widetilde{H}^{\beta\alpha}_{s,off} \widetilde{H}^{\alpha\beta}_{s,off}(-\tau) \rangle + \langle \widetilde{H}^{\beta\alpha}_{s,off} \widetilde{H}^{\alpha\beta}_{sb,off}(-\tau) \rangle \\ &+ \langle \widetilde{H}^{\beta\alpha}_{sb,off} \widetilde{H}^{\alpha\beta}_{s,off}(-\tau) \rangle + \langle \widetilde{H}^{\beta\alpha}_{sb,off} \widetilde{H}^{\alpha\beta}_{sb,off}(-\tau) \rangle \} \\ &= R^{FT}_{\alpha\beta}(t) + R^{mRT}_{\alpha\beta}(t) + 2R^{cross}_{\alpha\beta}(t), \end{aligned} \tag{2.36}$$

contains four parts after expanding, a FT-term caused by electronic coupling $H_{s,off}$, a mRT-term by electron-phonon coupling $H_{sb,off}$, and two cross-terms by mix perturbation.

These three terms can be evaluated:

$$R^{FT}_{\alpha\beta}(t) = 2|\widetilde{J}|^2 \cdot \mathrm{Re} \int_0^t d\tau F^*_\beta(\tau) A_\alpha(\tau), \tag{2.37}$$

$$R^{mRT}_{\alpha\beta}(t) = 2 \cdot \mathrm{Re} \int_0^t d\tau F^*_\beta(\tau) A_\alpha(\tau) X_{\alpha\beta}(\tau), \tag{2.38}$$

$$R^{cross}_{\alpha\beta}(t) = 2\widetilde{J} \cdot \mathrm{Re} \int_0^t d\tau F^*_\beta(\tau) A_\alpha(\tau) N_{\alpha\beta}(\tau), \tag{2.39}$$

doi:10.6342/NTU202404389

where

$$A_\alpha(t) = \exp\{-i\epsilon_\alpha t - g_{\alpha\alpha\alpha\alpha}(t)\}, \tag{2.40}$$

$$F_\beta(t) = \exp\{-i(\epsilon_\beta - 2\lambda_{\beta\beta\beta\beta})t - g_{\beta\beta\beta\beta}(t)\}, \tag{2.41}$$

which are associated with absorption and emission lineshape respectively. Furthermore, the complicated $X(t)$ and $N(t)$ describe the mixing dynamics of $|\alpha\rangle$ and $|\beta\rangle$ induced by phonons and can be evaluated to yield

$$\begin{aligned} X_{\alpha\beta}(t) = \exp\{2(g_{\alpha\alpha\beta\beta}(t) + i\lambda_{\alpha\alpha\beta\beta}t)\} \\ \times [\ddot{g}_{\beta\alpha\alpha\beta}(t) - (\dot{g}_{\beta\alpha\alpha\alpha}(t) - \dot{g}_{\beta\alpha\beta\beta}(t) - 2i\lambda_{\beta\alpha\beta\beta}) \\ \times (\dot{g}_{\alpha\beta\alpha\alpha}(t) - \dot{g}_{\alpha\beta\beta\beta}(t) - 2i\lambda_{\alpha\beta\beta\beta})] , \end{aligned} \tag{2.42}$$

$$\begin{aligned} N_{\alpha\beta}(t) = \exp\{2(g_{\alpha\alpha\beta\beta}(t) + i\lambda_{\alpha\alpha\beta\beta}t)\} \\ \times [i\left(-\dot{g}_{\beta\alpha\alpha\alpha}(t) + \dot{g}_{\beta\alpha\beta\beta}(t)\right) - 2\lambda_{\beta\alpha\beta\beta}] . \end{aligned} \tag{2.43}$$

For the reference system is exactly localized site basis corresponding to θ=0, the transfer rate is determined by the FT-term only, which is equivalent to the Förster theory, because the coefficient $C_n^\alpha C_n^\beta$ in the mRT-term and cross term equals to zero. The coefficient $C_n^\alpha C_n^\beta$ represents the overlap of $|\alpha\rangle$ and $|\beta\rangle$ at the local n-th site. In contrast, the reference system which is chosen at the electronic eigenstate produces only the mRT-term, which is the same as in the modified Redfield theory because the $\widetilde{J}$ in the FT-term and cross-term is zero at the electronic eigenstate. However, in an intermediate electronic basis, the unique cross-term is important as it represents the non-trivial effect between $|\alpha\rangle$ and $|\beta\rangle$ that is not adequately described by either FT or CMRT.

doi:10.6342/NTU202404389

doi:10.6342/NTU202404389

Chapter 3 Variational Polaron Eletronic reference states

3.1 Partial Polaron Transformation

Because the bath could affects the system, we apply a variational polaron transformation[21, 24, 25] representing the phenomenon of distorted phonon cloud on H to describe the interaction between system and bath. Therefore, we take advantage of the eigenbasis of this variational polaron system Hamiltonian to be our reference system.

$$H' = e^{S} H e^{-S} \tag{3.1}$$

$$S = -f \sum_{n,i} g_{ni} (b_{ni} - b_{ni}^{\dagger}) |n\rangle\langle n|, \tag{3.2}$$

where f is a dimensionless parameter between 0 and 1 corresponding to original undistorted basis and fully displaced small polaron transformation respectively.

doi:10.6342/NTU202404389

3.1.1 System Hamiltonian

After evaluated, we obtain $H' = H'_s + H'_b + H'_{sb}$ and the system part is

$$H'_s = [-f\,(2-f)\,\lambda_D + \Delta]\,|D\rangle\langle D| + [-f\,(2-f)\,\lambda_A - \Delta]\,|A\rangle\langle A| + J_{\text{eff}}(|D\rangle\langle A| + |A\rangle\langle D|), \tag{3.3}$$

where $\lambda_n = \sum_i g_{ni}^2 \omega_{ni}$ is reorganization energy for *n*th site, and

$$J_{\text{eff}} = J_0 \langle \theta_D^\dagger \theta_A \rangle, \tag{3.4}$$

is the effective coupling which represents the realistic electronic coupling after consider the phonon effect. $\theta_n = \exp\left\{ f \sum_i g_{ni}(b_{ni} - b_{ni}^\dagger) \right\}$, is a phonon displacement operator for the nth site, and $\langle \theta_D^\dagger \theta_A \rangle$ is a Franck-Condon factor which evaluated by thermal average to yield

$$\begin{aligned} \langle \theta_D^\dagger \theta_A \rangle &= \exp\left\{ -\frac{1}{2} \sum_i f^2 (g_{Di} - g_{Ai})^2 \coth\left(\frac{\beta\omega_i}{2} \right) \right\} \\ &= \exp\{ -f^2 \int_0^\infty d\omega \frac{J(\omega)}{\omega^2} \coth\left(\frac{\beta\omega}{2} \right) \} \end{aligned} \tag{3.5}$$

Owing to the displacement of phonon representing a relax process, the site energies decrease by a set of reorganization energies if f=1. Meanwhile, the electronic coupling is depressed because the overlap of phonons decreases.

doi:10.6342/NTU202404389

3.1.2 Bath and System-Bath Hamiltonian

The bath Hamiltonian is also the same as H_b, and the system-bath part is

$$H'_{sb} = J_0\left(\theta_D^\dagger\theta_A - \langle\theta_D^\dagger\theta_A\rangle\right)|D\rangle\langle A| + J_0\left(\theta_A^\dagger\theta_D - \langle\theta_A^\dagger\theta_D\rangle\right)|A\rangle\langle D| + \sum_i(1-f)g_{Di}\omega_{Di}(b_{Di}^\dagger + b_{Di})|D\rangle\langle D| + \sum_i(1-f)g_{Ai}\omega_{Ai}(b_{Ai}^\dagger + b_{Ai})|A\rangle\langle A|. \tag{3.6}$$

The former part of H'_{sb} is fluctuation of effective coupling by phonons and the latter part is site energy fluctuation caused by motion of phonon.

3.2 Bogoliubov Variational approximation

3.2.1 Variational Method to Determine Dressing Coefficient

In order to determine an appropriate f,we utilize the Bogoliubov's theorem which yield a free energy upper bond by partition the H' into H'_0 and V'.

$$A'_H \leq A_{H'_0} + \langle V'\rangle_{H'_0}, \tag{3.7}$$

We treat the H'_s and H'_b as H'_0, and H'_{sb} as V' and the energy bond can be evaluated to yield

$$A_{H'_0} = -\beta^{-1}\ln \mathrm{Tr}\left\{e^{-\beta H'_0}\right\}, \tag{3.8}$$

$$= -f(2-f)\int_0^\infty \frac{J(\omega)}{\omega}d\omega - \frac{1}{\beta}\ln\left[2\cosh\left(\beta\sqrt{\Delta^2 + J_{\text{eff}}^2}\right)\right], \tag{3.9}$$

doi:10.6342/NTU202404389

and $\langle V' \rangle_{H_0'} = 0$. Equation 3.9 represents the free energy evaluated by H_0', which is divided into two parts. The former is the reorganization energy component. When f equals 1, the total energy decreases by the amount of the reorganization energy. Conversely, when f is zero, this term does not contribute to the total energy. The latter is the electronic component which consist of β, Δ and J_{eff}. When f increases, J_{eff} decreases and Δ and β do not change. Moreover, since the average of perturbation is zero, we use the zeroth order Hamiltonian part to determine a most favorable f based on the competition between two parts of H_0. By solving $\frac{\partial A_{H_0'}}{\partial f} = 0$, yield

$$f = \left[1 + \frac{J_{\text{eff}}^2 \tanh\left(\beta\sqrt{\Delta^2 + J_{\text{eff}}^2}\right) \int_0^\infty d\omega \frac{J(\omega)}{\omega}}{\sqrt{\Delta^2 + J_{\text{eff}}^2} \int_0^\infty d\omega \frac{J(\omega)}{\omega^2} \coth\left(\frac{\beta\omega}{2}\right)} \right]^{-1} . \tag{3.10}$$

We show how the dressing coefficient f changes with J_0 in Fig.3.1. Initially, f remains close to 1 as J_0 increases. Around $J_0 = 1.2$, f begins to decrease rapidly, with a significant decline occurring between J_0 values of approximately 1.5 and 2.0. Beyond $J_0 = 2.0$, the rate of decrease in f slows down, and the curve gradually levels off. As J_0 approaches 3, f stabilizes around a value close to 0.2. Overall, Fig.3.1 illustrates a nonlinear decrease in f as J_0 increases, with a pronounced transition region where f drops sharply between J_0 values of 1.5 and 2.0.

3.2.2 Discussion of Energy Surfaces

Figure 3.2 illustrates the energy surface calculated from the Bogoliubov energy upper bound. The red line represents the reorganization energy part, the blue line represents the electronic part, and the black line represents the total energy in Eq.2.36 and the parameters for both panels are $\Delta = 1$, $\gamma = 1$, and $\beta = 0.5$. Panel (a) shows the case where $J_0 = 0.5$.

doi:10.6342/NTU202404389

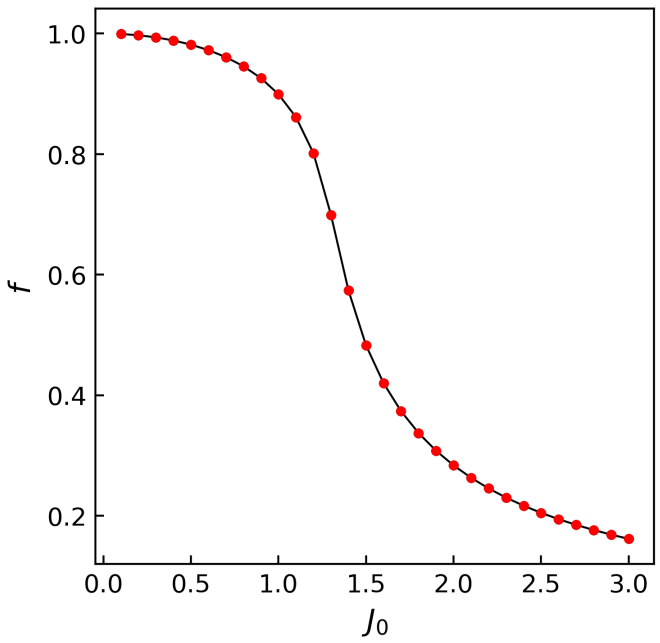

Figure 3.1: The dressing coefficient f as a function of J_0. $\Delta = 1, \beta = 0.5$ and $\gamma = 1$.

In this scenario, the reorganization energy component decreases as f increases, following a quadratic function. However, the electronic component increases slightly due to the very small value of J_0. Therefore, similar to the trend observed in the reorganization energy component, the total energy decreases significantly with increasing f, primarily driven by the reduction in the reorganization energy component. In conclusion, when f approaches 1, it is most favorable in terms of energy due to the dominance of the reorganization energy.

Panel (b) depicts the case where $J_0 = 2.5$. Here, the reorganization energy component also decreases as f increases, following a quadratic function, which Will not be affected by changes in J_0. Nevertheless, the electronic component increases as f increases more sharply than the case of $J_0 = 0.5$. Thus, the total energy initially decreases and then increases as f increases. The most favorable f is approximately 0.25, which is much smaller than the case for $J_0 = 0.5$ because of the dominance of the electronic component.

doi:10.6342/NTU202404389

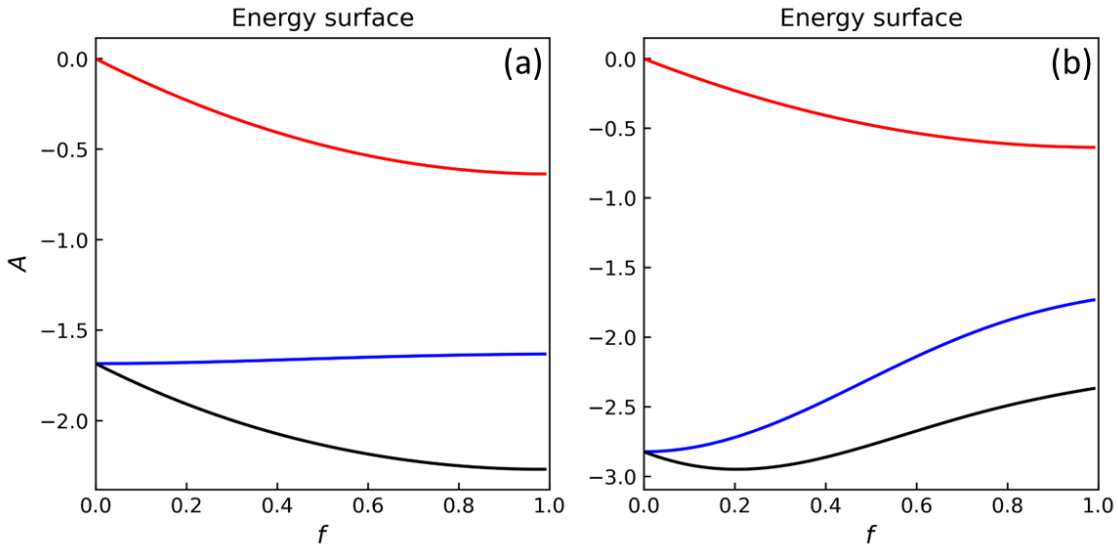

Figure 3.2: Energy surface calculated from the Bogoliubov energy upper bond. Red line: reorganization energy component, blue line: electronic component, and black line: total energy. (a)$J_0 = 0.5$, (b)$J_0 = 2.5$, and other parameters: $\Delta = 1, \gamma = 1$ and $\beta = 0.5$.

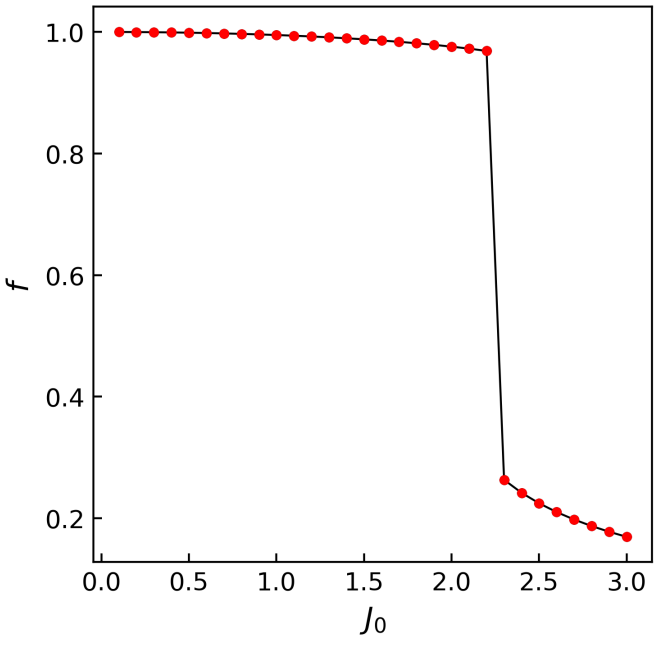

Figure 3.3: The dressing coefficient f as a function of J_0. $\Delta = 1, \beta = 0.5$ and $\gamma = 2$.

doi:10.6342/NTU202404389

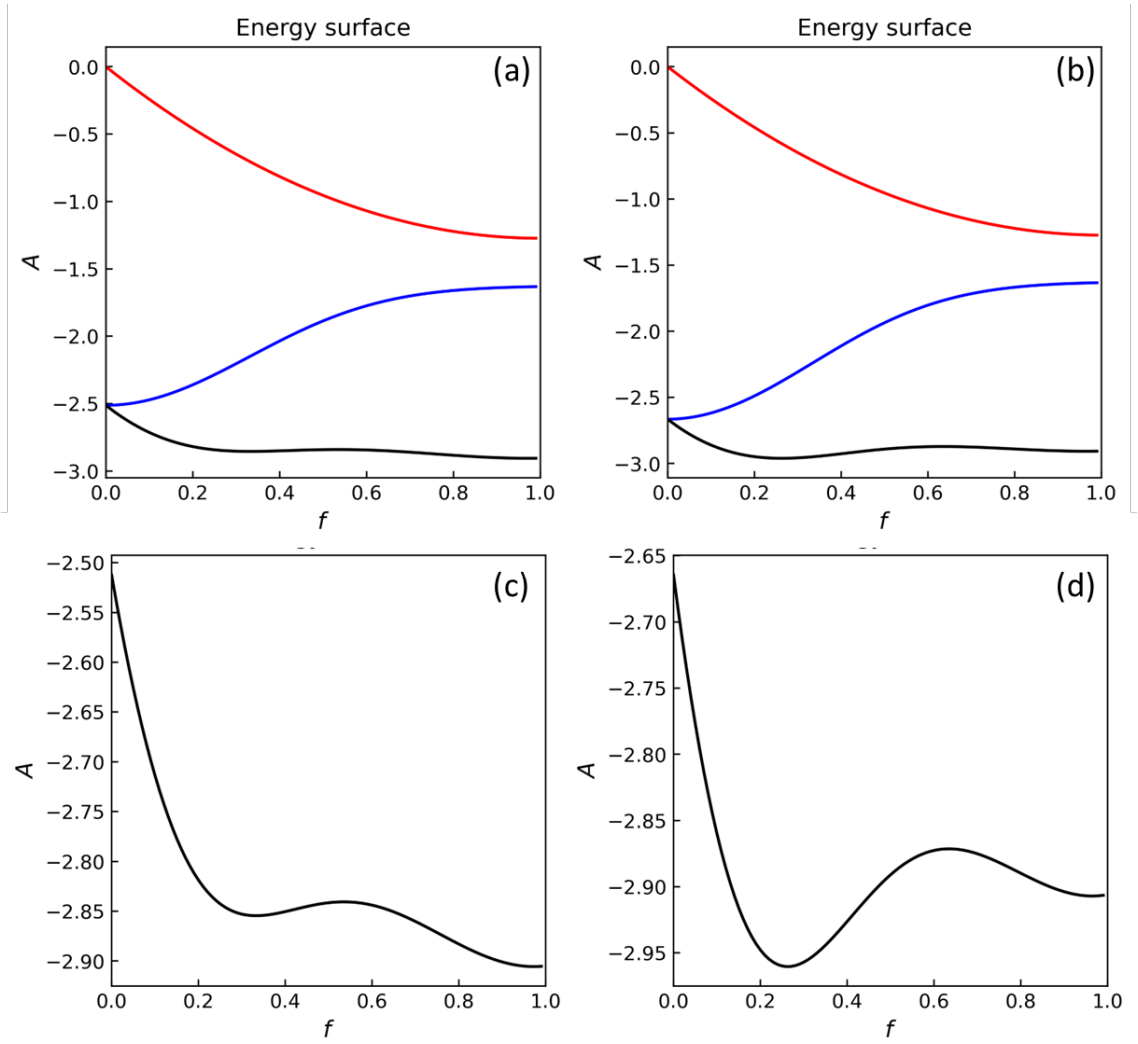

Figure 3.4: Energy surface calculated from the Bogoliubov energy upper bond. Red line: reorganization energy component, blue line: electronic component, and black line: total energy. (a)$J_0 = 2.1$, (b)$J_0 = 2.3$ and other parameters: $\Delta = 1, \gamma = 2$ and $\beta = 0.5$. Figure (c) and Figure (d) are the detail of total energy of Fig.(a) and Fig.(b).

doi:10.6342/NTU202404389

3.2.3 Abrupt Transition

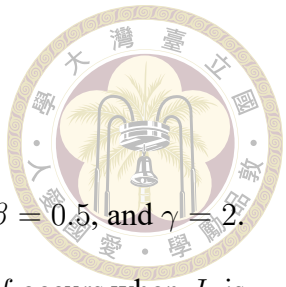

Figure 3.3 shows f as a function of J_0 in a system with $\Delta = 1$, $\beta = 0.5$, and $\gamma = 2$. As J_0 increases, f decreases slowly. However, an abrupt transition of f occurs when J_0 is approximately equal to 2.2 due to the shift of the global minimum from one local minimum to another[21, 24], as shown in Figure 3.4. After the transition point, f stabilizes around a value close to 0.2.

Figure 3.4 presents the energy surfaces at $J_0 = 2.1$ and $J_0 = 2.3$ in panels (a) and (b), respectively, with other parameters being the same as in Figure 3.3. The curves for the reorganization energy component are the same in both panels, but the electronic component in panel (b) is larger than in panel (a). Panels (c) and (d) show parts of the total energy, corresponding to the total energy curves in panels (a) and (b). These two graphs depict a double well of the energy surface. The global minimum in panel (c) is around $f = 1$, while the global minimum in panel (d) is around $f = 0.3$. As a result, the switch of the global minimum causes the abrupt transition seen in Figure 3.3.

After determining f, we obtain J_{eff} which is dressed by phonons and incorporates the dynamical localization effect.

3.3 Variational polaron reference system

Finally, we choose the eigenstates of H_s' as our electronic reference system used in our QME. Note that we do not use the polaron basis, which is a combination of electronic and vibronic states, but only borrow J_{eff} to perform a unitary transformation on the system Hamiltonian. We define θ_P as the mixing angle of our pure dephasing variational polaron

doi:10.6342/NTU202404389

reference system (PDVPRS) which can be evaluated by

$$\theta_P = \frac{1}{2} tan^{-1}(\frac{|J_{\text{eff}}|}{\Delta}), \tag{3.11}$$

and the mixing angle of CMRT is

$$\theta_R = \frac{1}{2} tan^{-1}(\frac{|J_0|}{\Delta}). \tag{3.12}$$

As J_{eff} becomes smaller, θ_P also becomes smaller which means the picture is more like FT. Otherwise, the J_{eff} is almost indistinguishable from J_0, so the picture is pretty similar to CMRT which is the eigenstate of system.

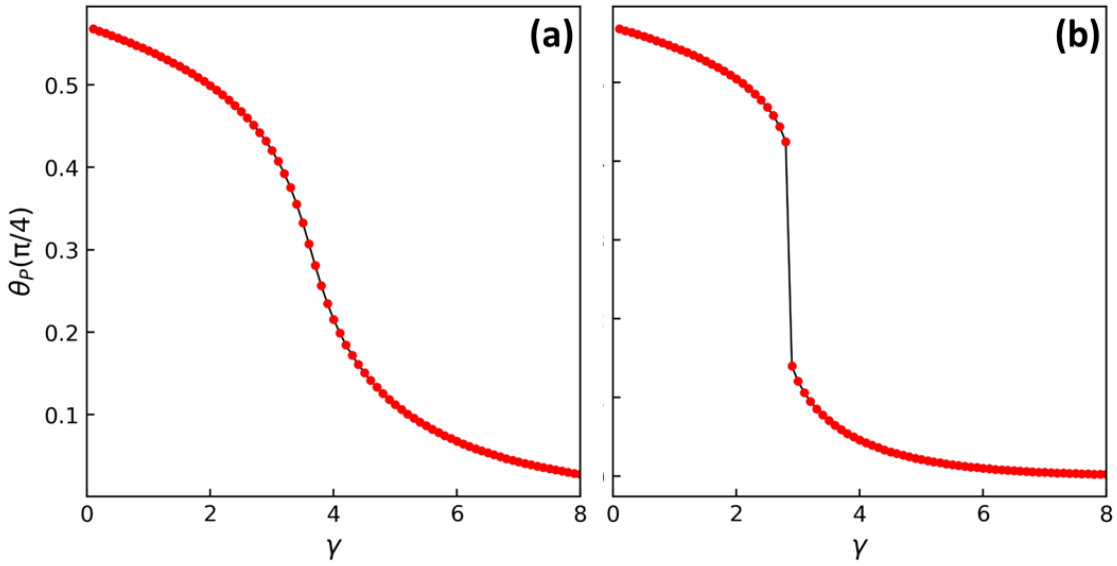

Figure 3.5: Mixing angle as a function of γ at different temperatures, (a) $\beta\omega_c$=4, (b) $\beta\omega_c$=1. Other parameter are Δ/ω_c=1 and J_0/ω_c=2.

3.3.1 Effects of System-Bath Coupling and Temperature

We first investigate the variational polaron reference system that depends on various system parameters. The reference system is defined by a mixing angle θ_P. Figure 3.5 shows θ_P as a function of γ in systems characterized by Δ/ω_c=1, J_0/ω_c=2, a typical

doi:10.6342/NTU202404389

electronically coupled dimer. In the figures, the vertical axis is scaled in units of $\frac{\pi}{4}$, which represents the maximum achievable mixing angle. We show the results at two different temperature. At both temperature, θ_P transition from large to small when γ increases corresponding to a transition from delocalized to localized reference system, respectively. Moreover, the transition at low temperatures occurs at a higher γ compared to that at high temperatures, as expected, due to increased thermal fluctuations at higher temperatures, which facilitate the transition. Clearly, PDVPRS captures the dynamical localization effect which causes localized system by dynamical fluctuation of bath[11].

The curves of θ_P as a function of γ is a smooth transition at low temperature. However, at high temperature, it becomes an abrupt transition which is an artifact of variational small polaronic ansatz because the optimal f shifts from one one local minimum to another. This issue could be improved by more sophisticated variational polaron approach[21, 27].

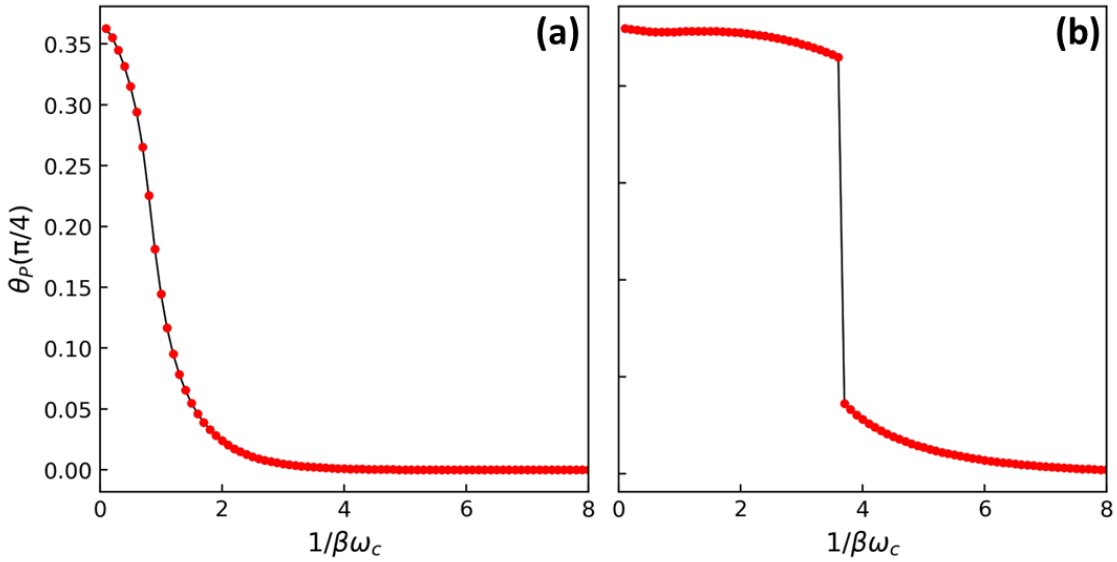

Figure 3.6: Mixing angle as a function of $1/\beta\omega_c$, (a) γ=2.5, (b) γ=1. Other parameters are Δ/ω_c=2, J_0/ω_c=2.

However, the temperature effect can be more clearly illustrated in Fig.3.6. Figure3.6 shows θ_P as a function of temperature at Δ/ω_c=2, J_0/ω_c=2 with different γ. As tempera-

doi:10.6342/NTU202404389

ture increases, θ_P decreases from a delocalized system to a localized system which can be attributed to the dynamical localization effect. Moreover, the θ_P decreases quickly at large γ in Fig.3.6(b) while at small γ , θ_P decreases slowly and exhibits an abrupt transition in Fig.3.6(b).

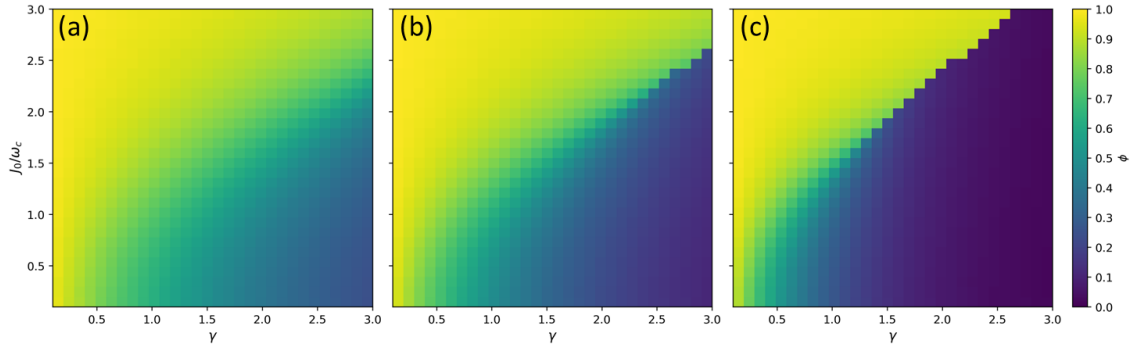

Figure 3.7: Mixing angle ratio ϕ as a function of γ and J_0/ω_c. Other parameters: Δ/ω_c=2 and (a) $\beta\omega_c$=2, (b) $\beta\omega_c$=1, (c) $\beta\omega_c$=0.5.

3.3.2 Quantifying the Deviation of PDVPRS from Conventional Approaches

To better quantify the deviation of the PDVPRS from the Redfield picture, we define a mixing angle ratio,

$$\phi = \frac{\theta_P}{\theta_R}. \tag{3.13}$$

In this definition, ϕ has a value between 0 and 1. When ϕ=0, the reference system corresponds to the localized Förster picture, whereas when ϕ=1, the reference system is the electronic eigenstates used in the Redfield picture.

Figure3.7 illustrates the relationship between ϕ and J_0/ω_c and γ and provides a visual representation of how ϕ varies with changes in J_0/ω_c and γ where the x-axis represents γ ranging from 0 to 3 and the y-axis represents J_0, also ranging from 0 to 3. For panel (a), at a low temperature regime, the reference system aligns closely with the Redfield picture

doi:10.6342/NTU202404389

for $J_0/\omega_c > \gamma$. Otherwise, for $J_0/\omega_c < \gamma$, the PDVPRS exhibits an intermediate basis different from conventional Redfield picture or Förster picture. In this regime, PDVPRS-QME is different from CMRT and FT and involved the dynamics of the cross term in Eq.2.39. Moreover, abrupt transition do not occur in the low temperature system.

For panel (b), the temperature is higher than panel (a). For very small values of γ, the reference system aligns closely with the Redfield picture, independent of the magnitude of J_0. Conversely, for large values of γ, the system predominantly adheres to a localized basis owing to the dynamical localization effect, and undergoes an abrupt transition to the Redfield picture unless J_0 is sufficiently large. In general, ϕ approaches 1 when $J_0 > \gamma$, and conversely, ϕ approaches 0 when $J_0 < \gamma$. However, when the magnitudes of J_0/ω_c and γ have a marginal difference, ϕ settles at an intermediate value, and the reference system adopts an intermediate basis.

Finally, the panel (c) shows ϕ as a function of γ and J_0/ω_c at highest temperature. The panel exhibits a similar overall trend; however, the transition occurs at a larger J_0 value, and the region of abrupt transition is also more extensive.

doi:10.6342/NTU202404389

Chapter 4 PDVPRS-QME Dynamics

4.1 Benchmarking of PDVPRS-QME Dynamics

4.1.1 Comparison with Conventional Theories

In this section, we benchmark PDVPRS-QME results against results obtained from the numerically exact quasiadiabatic propagator path integral (QUAPI) method to determine the effectiveness of the new theory. The QUAPI data used in this paper is obtained from previous work of our group[23]. We also compare PDVPRS-QME with FT and CMRT to elucidate how the new theory improves on the conventional perturbative approaches.

First, we investigate the EET dynamics of a dimer system consisting of a donor and an acceptor at different system-bath coupling strengths. Figure 4.1 depicts the population dynamics calculated from PDVPRS-QME, CMRT, FT and QUAPI with different γ and Δ/ω_c=0.5, J_0/ω_c=0.5, $\beta\omega_c$=0.5. In Fig.4.1(a), γ is small, and PDVPRS-QME with ϕ=0.88 and CMRT show an oscillatory behavior induced by the zeroth-order Hamiltonian. The behavior is consistent with QUAPI result. Moreover, the relaxation calculated by PDVPRS-QME and CMRT matches exactly with the QUAPI results. Nevertheless, although FT can describe the population transfer, it does not capture any oscillatory be-

doi:10.6342/NTU202404389

havior in an incoherent picture. Therefore, PDVPRS-QME exhibits an excellent results by providing an appropriate reference system close to coherent Redfield picture in the weak system-bath coupling regime.

At a intermediate γ in fig. 4.1(b),compared to CMRT, PDVPRS-QME demonstrate results that are reasonably similar to those obtained with QUAPI as well as FT but PDVPRS-QME has a slight detailed balance problem. Moreover, CMRT mildly overestimates the population transfer rate and exhibits noticeable oscillatory behavior at early times, whereas QUAPI does not. Generally, the three theories perform acceptably in the intermediate γ regime, indicating that the results are not sensitive to the choice of reference system and that all pictures are applicable.

In Figure 4.1(c), PDVPRS-QME using a localized picture ($\phi = 0.1$) and FT yield results that are nearly identical to those obtained with QUAPI. In the strong system-bath coupling regime, coherent transfer is suppressed due to the dynamical localization effect, which undermines the system's delocalization. In contrast, CMRT are always in the eigenstate of system but does not consider the dynamical localization effect which is important at strong system-bath coupling. Therefore, CMRT overestimates the population transfer rate owing to an improperly over-delocalized basis. Figure 4.1 shows that PDVPRS-QME has broader applicability for various γ and bridges the CMRT(coherent regime) and FT(incoherent regime) by variational polaron approach to determine an appropriate basis.

Furthermore, we show the temperature dependence of population dynamics at a small Δ/ω_c in Fig.4.2. At low temperature in Fig.4.2(a), PDVPRS-QME and CMRT exhibit an oscillatory behavior like Fig.4.1(a) but there is a noticeable bias of oscillation frequency[11]. Förster theory can not capture this oscillatory dynamics. Generally speaking,

doi:10.6342/NTU202404389

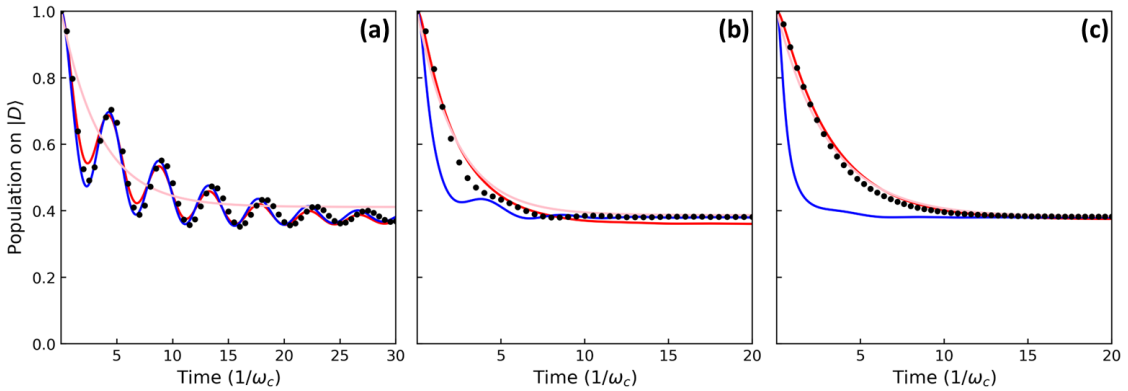

Figure 4.1: Population dynamics calculated with PDVPRS-QME (red line), CMRT (blue line), FT (pink line), QUAPI (dots) in a high temperature bath with different γ, (a)γ=0.2, (b)γ=1, (c)γ=2. Other parameters are Δ/ω_c=0.5, J_0/ω_c=0.5 and $\beta\omega_c$=0.5. The mixing angle ratio ϕ: (a)0.88, (b)0.35, (c)0.1.

PDVPRS-QME and CMRT are better method to describe dynamics in a small biased system at low temperature.

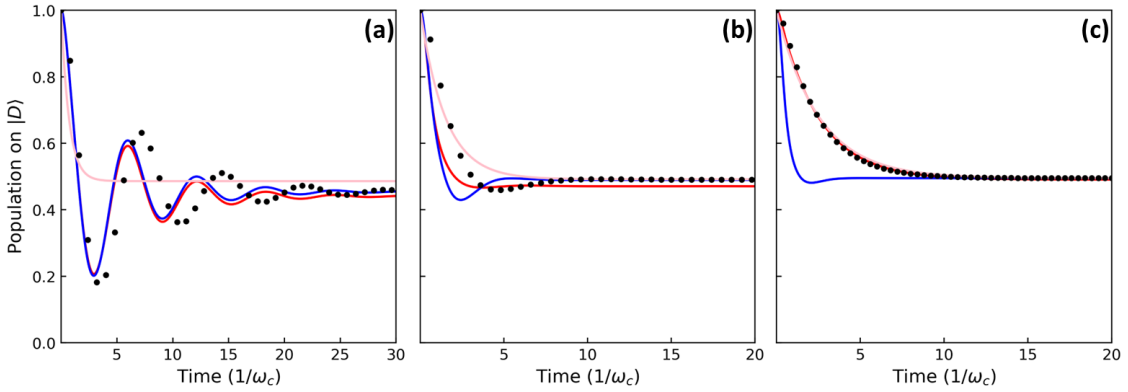

Figure 4.2: Population dynamics calculated with PDVPRS-QME (red line), CMRT (blue line), FT (pink line), QUAPI (dots) in a a small Δ/ω_c regime with different $\beta\omega_c$, (a)$\beta\omega_c$=1, (b)$\beta\omega_c$=0.2, (c)$\beta\omega_c$=0.1. Other parameters are Δ/ω_c=0.1, J_0/ω_c=0.5 and γ=0.5.The mixing angle ratio ϕ: (a)0.96, (b)0.59, (c)0.15.

At a higher temperature, Fig.4.2(b) shows three theories have evident discrepancies with QUAPI but PDVPRS-QME with ϕ=0.59 exhibits more realistic results compared to CMRT and FT. Accordingly, cross term plays an important role in the intermediate regime which can not be described by Redfield picture or Förster picture.

In Fig.4.2(c), we show that PDVPRS-QME with ϕ=0.15 can exactly captures the population transfer dynamics compared to QUAPI as well as FT in an incoherent picture

doi:10.6342/NTU202404389

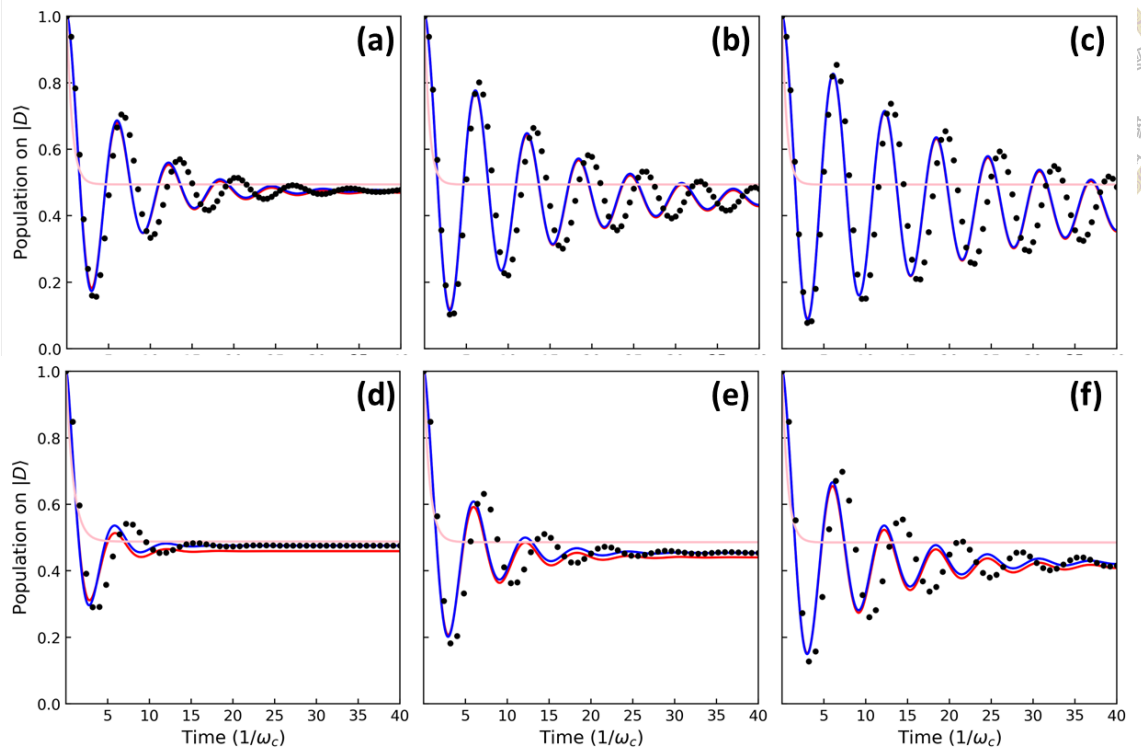

Figure 4.3: Population dynamics calculated with PDVPRS-QME (red line), CMRT (blue line), FT (pink line), QUAPI (dots) in a a small Δ/ω_c regime with different γ and $\beta\omega_c$, (a) $\gamma = 0.2$, $\beta\omega_c = 0.5$, (b) $\gamma = 0.2$, $\beta\omega_c = 1$, (c) $\gamma = 0.2$, $\beta\omega_c = 2$, (d) $\gamma = 0.5$, $\beta\omega_c = 0.5$, (e) $\gamma = 0.5$, $\beta\omega_c = 1$ and (f) $\gamma = 0.5$, $\beta\omega_c = 2$. Other parameters are Δ/ω_c=0.1 and J_0/ω_c=0.5.

at highest temperature. Moreover, the transfer rate is slower than Fig.4.2(b) owing to dynamical localization effect. However, CMRT overestimates the transfer rate with an improper delocalized basis in a small Δ system with high temperature[11, 13, 28]. From Fig.4.1 and Fig.4.2, PDVPRS-QME unifies the CMRT and FT as successfully identifies an optimal reference system while circumventing the problems inherent in the CMRT or FT by utilizing the PDVPRS approach.

We present a set of dynamics that align with a coherent picture in Fig.4.3. In this figure, γ and $\beta\omega_c$ are weak in general, and $\Delta = 0.1$, $J_0/\omega_c = 0.5$. The lower the temperature, the stronger the oscillation behaviors observed. Moreover, strong system-bath coupling destroys the oscillation dynamics. In this coherent system, FT cannot describe the oscillation behavior, but CMRT and PDVPRS-QME can.

doi:10.6342/NTU202404389

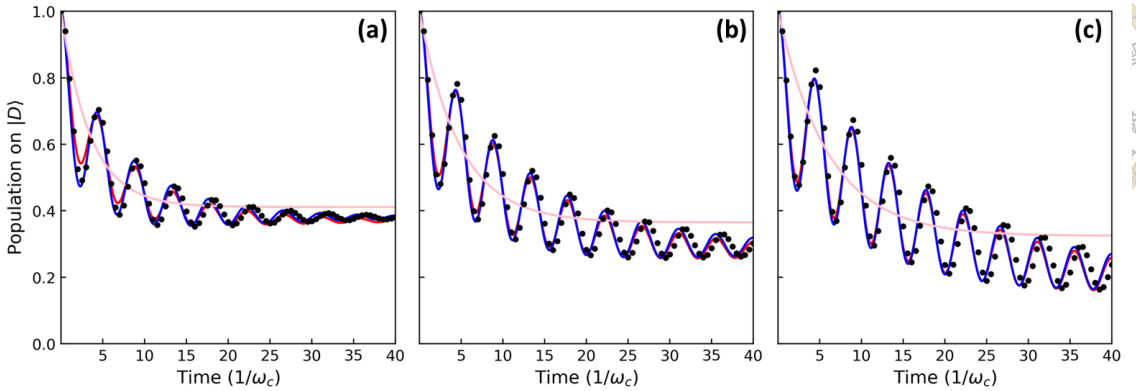

Figure 4.4: Population dynamics calculated with PDVPRS-QME (red line), CMRT (blue line), FT (pink line), QUAPI (dots) in a a small Δ/ω_c regime with different γ and $\beta\omega_c$, (a) $\gamma = 0.2$, $\beta\omega_c = 0.5$, (b) $\gamma = 0.2$, $\beta\omega_c = 1$ and (c) $\gamma = 0.2$ $\beta\omega_c = 2$. Other parameters are Δ/ω_c=0.5 and J_0/ω_c=0.5.

In Fig.4.4, we observe population dynamics with $\Delta/\omega_c = 0.5$ and $J_0/\omega_c = 0.5$ under different γ and $\beta\omega_c$ conditions. Specifically, (a) $\gamma = 0.2$, $\beta\omega_c = 0.5$, (b) $\gamma = 0.2$, $\beta\omega_c = 1$, and (c) $\gamma = 0.2$, $\beta\omega_c = 2$. The results indicate that as the temperature decreases, the oscillatory behavior becomes more pronounced. Here, FT fails to capture these dynamics, whereas CMRT and PDVPRS-QME accurately replicate the coherent oscillations observed in QUAPI.

Similarly, Fig.4.5 illustrates population dynamics with $\Delta/\omega_c = 0.5$ and $J_0/\omega_c = 1$. Again, the parameters $\gamma = 0.2$ and $\beta\omega_c$ take the values (a) 0.5, (b) 1, and (c) 2. The dynamics show consistent oscillatory behavior, especially at lower temperatures, which are well captured by CMRT and PDVPRS-QME, while FT continues to overestimate the population transfer rates.

In Fig.4.6, the dynamics for $\Delta/\omega_c = 0.5$ and $J_0/\omega_c = 2$ are presented. The conditions for γ and $\beta\omega_c$ remain the same: (a) 0.2, 0.5, (b) 0.2, 1, and (c) 0.2, 2. As with the previous figures, the oscillations become more apparent at lower temperatures, and once again, FT fails to accurately model these behaviors. CMRT and PDVPRS-QME continue to align closely with the results from QUAPI.

doi:10.6342/NTU202404389

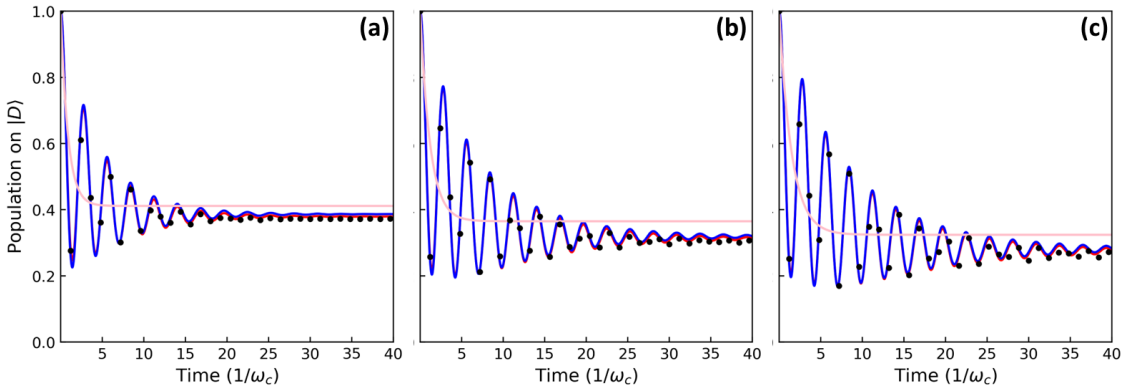

Figure 4.5: Population dynamics calculated with PDVPRS-QME (red line), CMRT (blue line), FT (pink line), QUAPI (dots) in a a small Δ/ω_c regime with different γ and $\beta\omega_c$, (a) $\gamma = 0.2$, $\beta\omega_c = 0.5$, (b) $\gamma = 0.2$, $\beta\omega_c = 1$ and (c) $\gamma = 0.2$ $\beta\omega_c = 2$. Other parameters are Δ/ω_c=0.5 and J_0/ω_c=1.

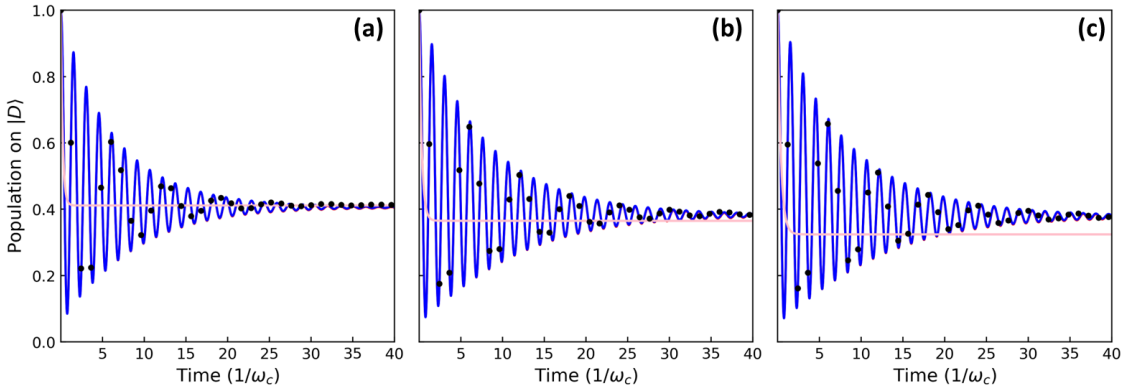

Figure 4.6: Population dynamics calculated with PDVPRS-QME (red line), CMRT (blue line), FT (pink line), QUAPI (dots) in a a small Δ/ω_c regime with different γ and $\beta\omega_c$, (a) $\gamma = 0.2$, $\beta\omega_c = 0.5$, (b) $\gamma = 0.2$, $\beta\omega_c = 1$ and (c) $\gamma = 0.2$ $\beta\omega_c = 2$. Other parameters are Δ/ω_c=0.5 and J_0/ω_c=2.

doi:10.6342/NTU202404389

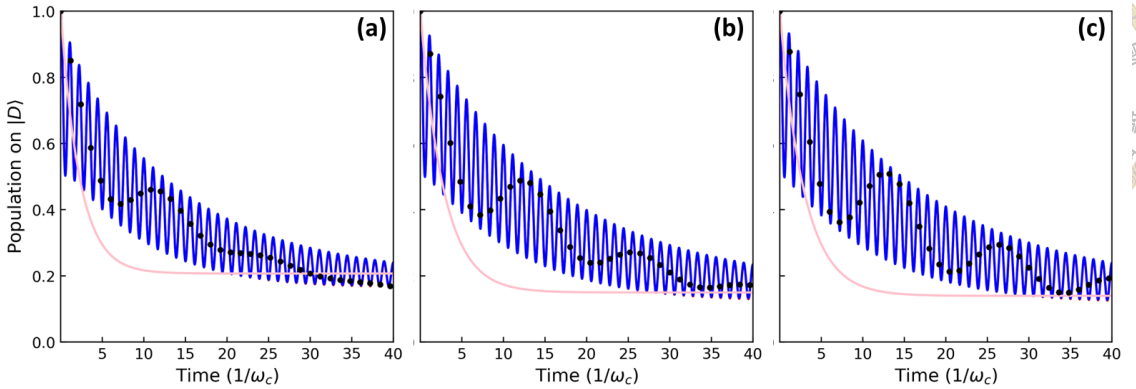

Figure 4.7: Population dynamics calculated with PDVPRS-QME (red line), CMRT (blue line), FT (pink line), QUAPI (dots) in a a small Δ/ω_c regime with different γ and $\beta\omega_c$, (a) $\gamma = 0.2$, $\beta\omega_c = 0.5$, (b) $\gamma = 0.2$, $\beta\omega_c = 1$ and (c) $\gamma = 0.2$ $\beta\omega_c = 2$. Other parameters are Δ/ω_c=2 and J_0/ω_c=2.

Lastly, Fig.4.7 presents the population dynamics with $\Delta/\omega_c = 2$ and $J_0/\omega_c = 2$. For this set of parameters, the behavior is evaluated under (a) $\gamma = 0.2$, $\beta\omega_c = 0.5$, (b) $\gamma = 0.2$, $\beta\omega_c = 1$, and (c) $\gamma = 0.2$, $\beta\omega_c = 2$. Here, the stronger system-bath coupling begins to suppress the coherent oscillations more significantly. Despite this, CMRT and PDVPRS-QME still provide accurate descriptions, whereas FT fails to capture the underlying dynamics.

4.1.2 Analysis of Downhill Decay Rates

Furthermore, We analyze the decay rates form donor to acceptor in a system with a small energy gap obtained by PDVPRS-QME, CMRT and FT. Here, we determine the rates by fitting the dynamics with a function given by:

$$F(t) = (1 - P^{\text{eq}}) \cos(\omega t) \exp(-t/\tau) + P^{\text{eq}} \tag{4.1}$$

where P^{eq} represents the equilibrium population, ω is the oscillatory frequency, and τ is the decay constant. In Fig. 4.8, the decay rates are calculated as $1/\tau$. The decay rate is a better indicator of how fast the population transfer within the original site basis compared

doi:10.6342/NTU202404389

to the population transfer rate in Eq. 2.28, as it considers both the population transfer and the dephasing of coherence in the reference system.

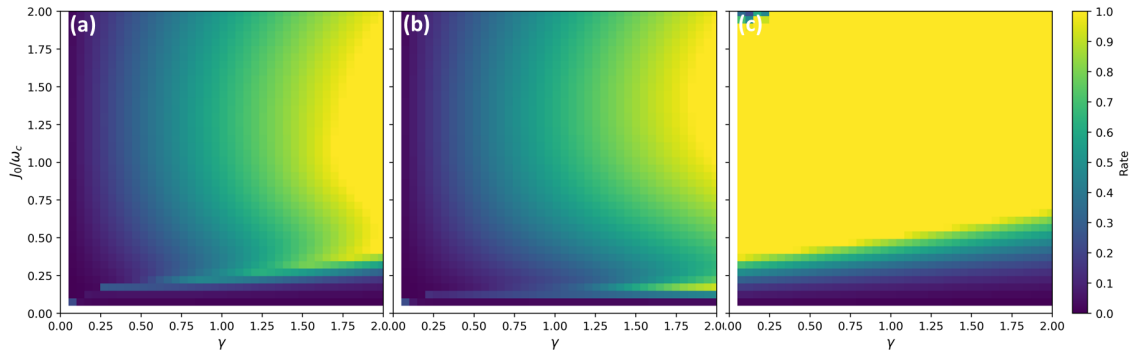

Figure 4.8: Downhill decay rates calculated with different theories as a function of γ and J_0/ω_c in a nearly degenerate system where Δ/ω_c=0.1, $\beta\omega_c$=1. (a) PDVPRS-QME, (b) CMRT, (c) FT.

For three theories, as J_0/ω_c increases, the rates increase as well. However, for CMRT, a noticeable area of higher values at the small J_0/ω_c in Fig.4.8(b) corresponding the well-known problem of the CMRT that overestimates the transfer rate at a near degenerate system. Nevertheless, in Panel (b) of Fig.4.8, PDVPRS-QME does not overestimate the rate in the regime that CMRT does not work because a consideration of dynamical localization effect by the variational polaron approach.

Furthermore, FT badly overestimates the transfer rate at large J_0/ω_c regime which is predictable because the perturbation is large inappropriate and the transfer rate in FT is proportional to $|J_0|^2$. However, PDVPRS-QME does not encounter this issue because PDVPRS provides a delocalized reference system as J_0/ω_c is large. Therefore, PDVPRS-QME avoids inherent problems associated with two conventional approaches.

doi:10.6342/NTU202404389

4.2 Unified Results for PDVPRS-QME with CMRT and FT: Localized Cases

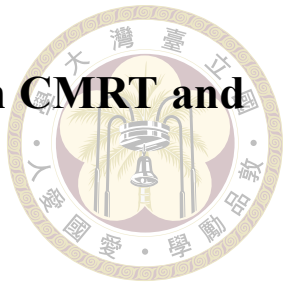

Figure 4.9 shows the dynamics with large Δ/ω_c where the eigenstates of these systems are quite localized ($\theta_R = 0.12$rad). In the scenario of small γ and low temperature, as depicted in Fig.4.9(a), the PDVPRS-QME with =0.82, CMRT, and FT all produce dynamics that align closely with QUAPI, suggesting a consistency among these approaches[10]. This convergence in results can be anticipated by considering the mixing angles in the PDVPRS-QME framework, where θ_R, θ_P and original basis are pretty close to each other leading to PDVPRS-QME providing analogous results across values of θ=θ_R (CMRT), θ_P (PDVPRS-QME) and 0 (FT). Additionally, under conditions of large γ and high temperatures, although the three theories yield consistent outcomes, they encounter a detailed balance issue. Moreover, from discussion of dynamics in this section, modified Redfield theory does not recover FT but only at large Δ/ω_c ($\Delta \gg J_0$).

Similar results are presented in Fig.4.10 and Fig.4.11 for larger J_0/ω_c compared to Fig.4.9. Due to the larger J_0/ω_c, θ has a wider range of variation. Therefore, while the results are not identical to the previous case, they still show a similar trend. In Fig.4.10, because γ and $\beta\omega_c$ are weak, the Förster Theory (FT) exhibits a noticeable deviation from other theories. However, for a stronger bath, as shown in Fig.4.11, FT yields results closer to those of the QUAPI method than to those of CMRT.

doi:10.6342/NTU202404389

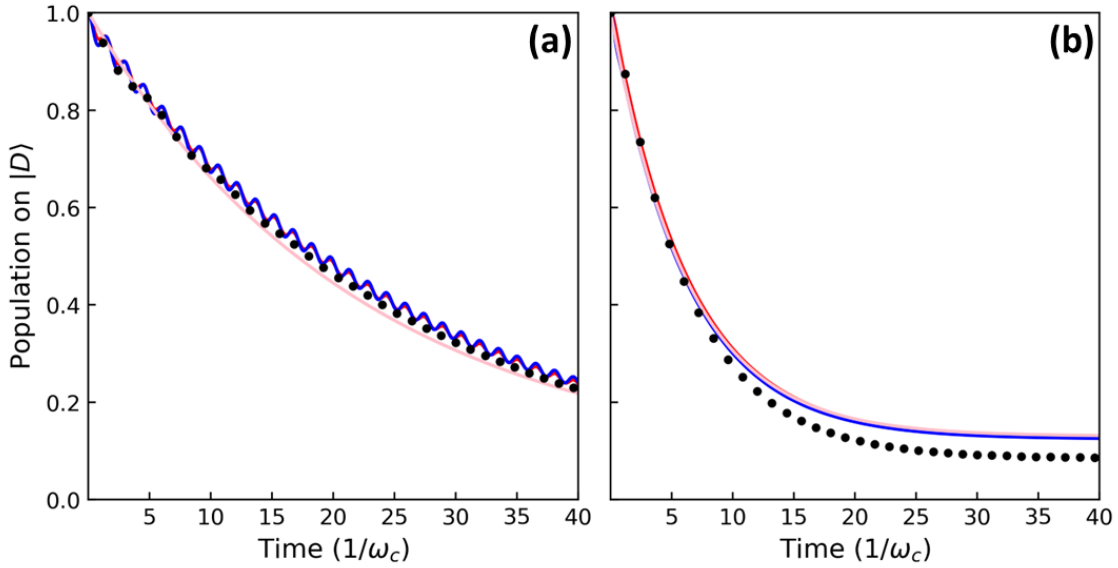

Figure 4.9: Population dynamics calculated with PDVPRS-QME (red line), CMRT (blue line), FT (pink line), QUAPI (dots) in a large Δ/ω_c regime with different γ and $\beta\omega_c$, (a)γ=0.5, $\beta\omega_c$=2, (b)γ=2, $\beta\omega_c$=0.5. Other parameters are Δ/ω_c=2 and J_0/ω_c=0.5.

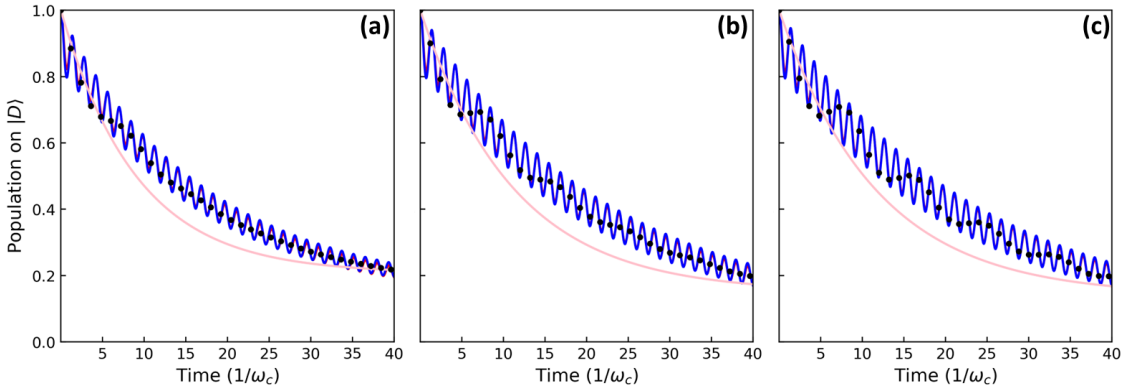

Figure 4.10: Population dynamics calculated with PDVPRS-QME (red line), CMRT (blue line), FT (pink line), QUAPI (dots) in a large Δ/ω_c regime with different γ and $\beta\omega_c$, (a) $\gamma = 0.2$, $\beta\omega_c = 0.5$, (b) $\gamma = 0.2$, $\beta\omega_c = 1$ and (c) $\gamma = 0.2$ $\beta\omega_c = 2$. Other parameters are Δ/ω_c=2 and J_0/ω_c=1.

doi:10.6342/NTU202404389

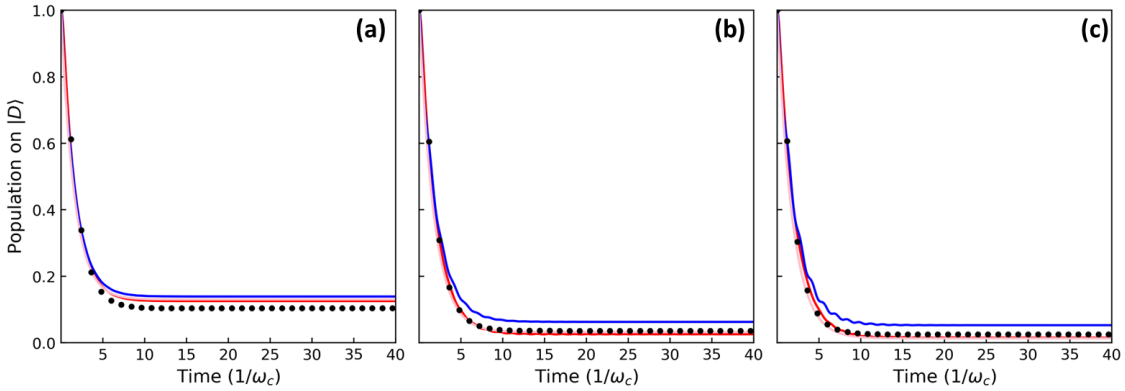

Figure 4.11: Population dynamics calculated with PDVPRS-QME (red line), CMRT (blue line), FT (pink line), QUAPI (dots) in a large Δ/ω_c regime with different γ and $\beta\omega_c$, (a) $\gamma = 2$, $\beta\omega_c = 0.5$, (b) $\gamma = 2$, $\beta\omega_c = 1$ and (c) $\gamma = 2$ $\beta\omega_c = 2$. Other parameters are Δ/ω_c=2 and J_0/ω_c=1.

doi:10.6342/NTU202404389

doi:10.6342/NTU202404389

Chapter 5 Intermediate Regime Analysis

5.1 Intermediate Regime Dynamics

Recalling Fig. 3.7, which presents a two-dimensional diagram of the mixing angle ratio, we focus our examination on the dynamics along the diagonal line. This diagonal represents the intermediate regime, where the mixing angles indicate a balance between localized and delocalized states. By analyzing the system's behavior in this region, we gain insight into how the dynamics evolve under conditions that are not fully captured by either extreme basis, thus highlighting the importance of considering intermediate bases for a comprehensive understanding of the system's behavior.

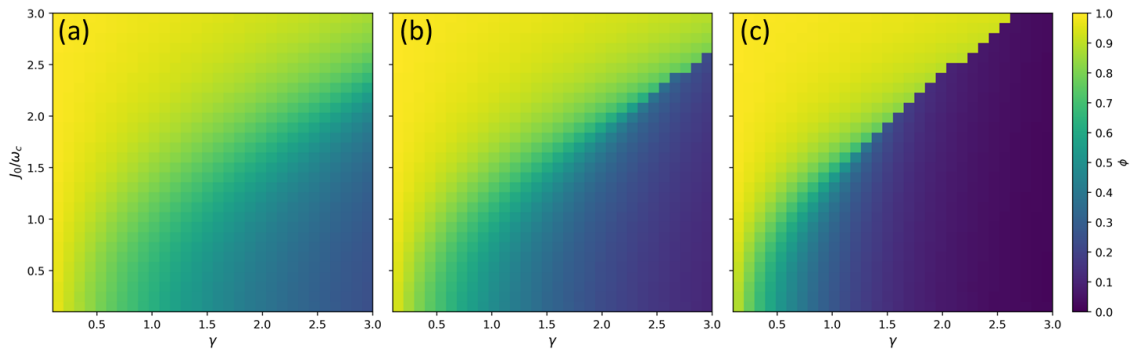

Figure 5.1: Mixing angle ratio ϕ as a function of γ and J_0/ω_c. Other parameters: Δ/ω_c=2 and $\beta\omega_c$=1.

doi:10.6342/NTU202404389

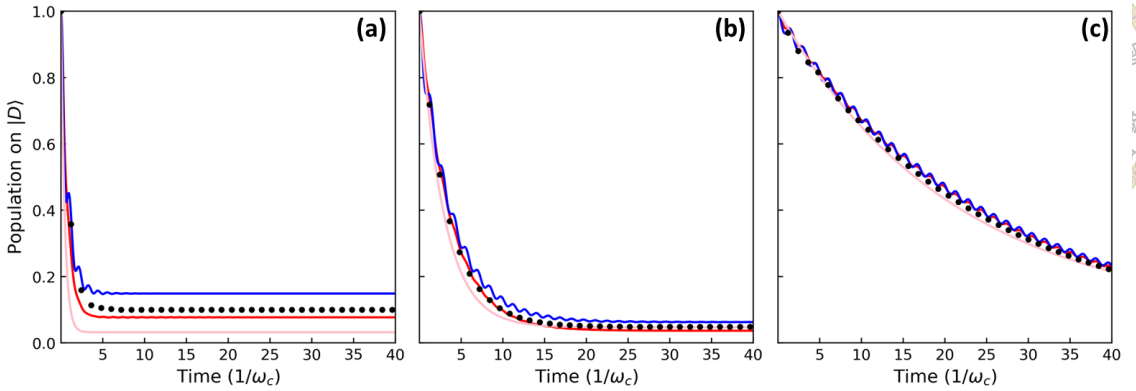

Figure 5.2: Population dynamics calculated with PDVPRS-QME (red line), CMRT (blue line), FT (pink line), QUAPI (dots) in the intermediate regime.(a)J_0/ω_c=2,γ=2, (b)J_0/ω_c=1,γ=1, (c)J_0/ω_c=0.5,γ=0.5. Other parameters: Δ/ω_c=2, $\beta\omega_c$=1.

For the 5.2(a), the dynamics in a system characterized by large J_0/ω_c and γ which are perturbation of CMRT and FT. Therefore, both CMRT and FT can't capture the realistic dynamics as expected. However, PDVPRS approach provides an intermediate reference system and PDVPRS-QME produces an consistent results with QUAPI by a properly mix perturbation which shows the importance of cross term. For the other two results, the weaker J_0/ω_c and γ, the more consistent with the three approach which is discussed in the section4.2. In conclusion, PDVPRS-QME exhibits broadened applicability across different regimes, avoiding limitations in traditional theories.

Figure **??** illustrates the dynamics within the intermediate regime where all parameters are set to 2. In this scenario, both CMRT and FT fail to accurately predict the system's behavior, particularly in estimating the detailed balance. Specifically, FT tends to overestimate the population transfer rates, which leads to an inaccurate portrayal of the energy transfer dynamics.

In contrast, PDVPRS-QME aligns precisely with the results obtained from QUAPI, demonstrating its ability to accurately capture the dynamics across various regimes. This figure clearly shows that PDVPRS-QME possesses a broader applicability across different

doi:10.6342/NTU202404389

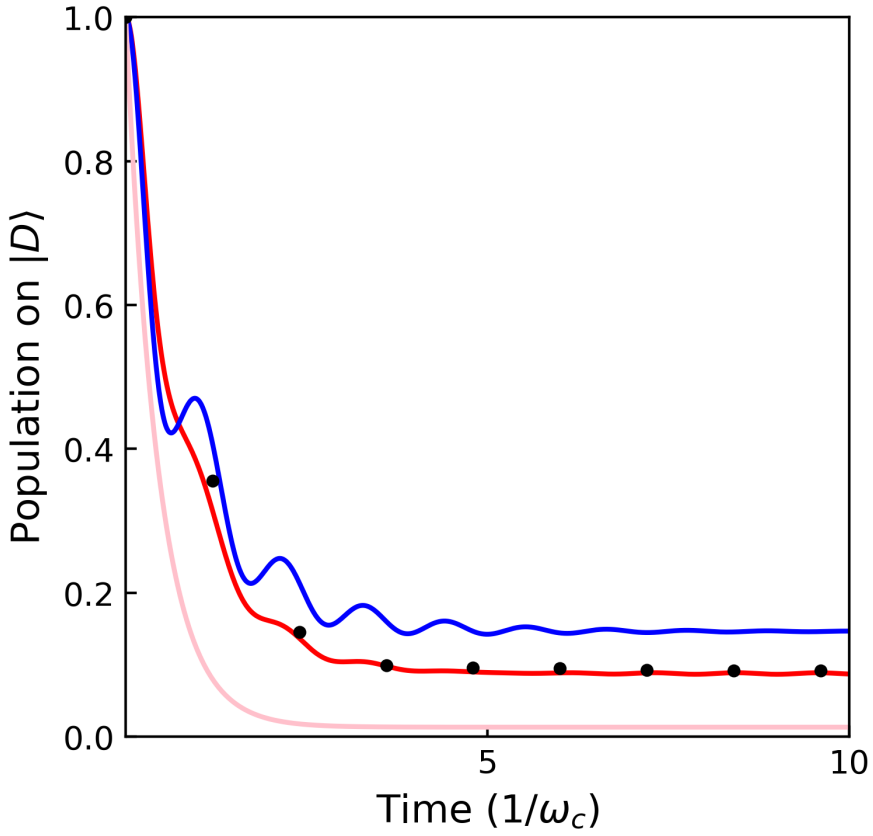

Figure 5.3: Population dynamics calculated with PDVPRS-QME (red line), CMRT (blue line), FT (pink line), QUAPI (dots) in the intermediate regime with J_0/ω_c=2,γ=2, Δ/ω_c=2, $\beta\omega_c$=2.

parameter sets due to its flexible and adaptive reference system. By properly accounting for both strong and weak electronic couplings through the appropriate choice of PDVPRS, this method provides a robust and reliable framework for studying complex quantum dynamics

5.2 Behavior of the PDVPRS-QME transfer rates

We analyse the transfer rate to clearly exhibit the behavior of PDVPRS-QME in different parameter regime and show the regime where the cross term is important. Figure 5.4 displays a series of two dimensional diagrams that illustrate the variation of Markovian rate terms of downhill transfer in Eq.2.36 as functions of γ and J_0/ω_c in a large

doi:10.6342/NTU202404389

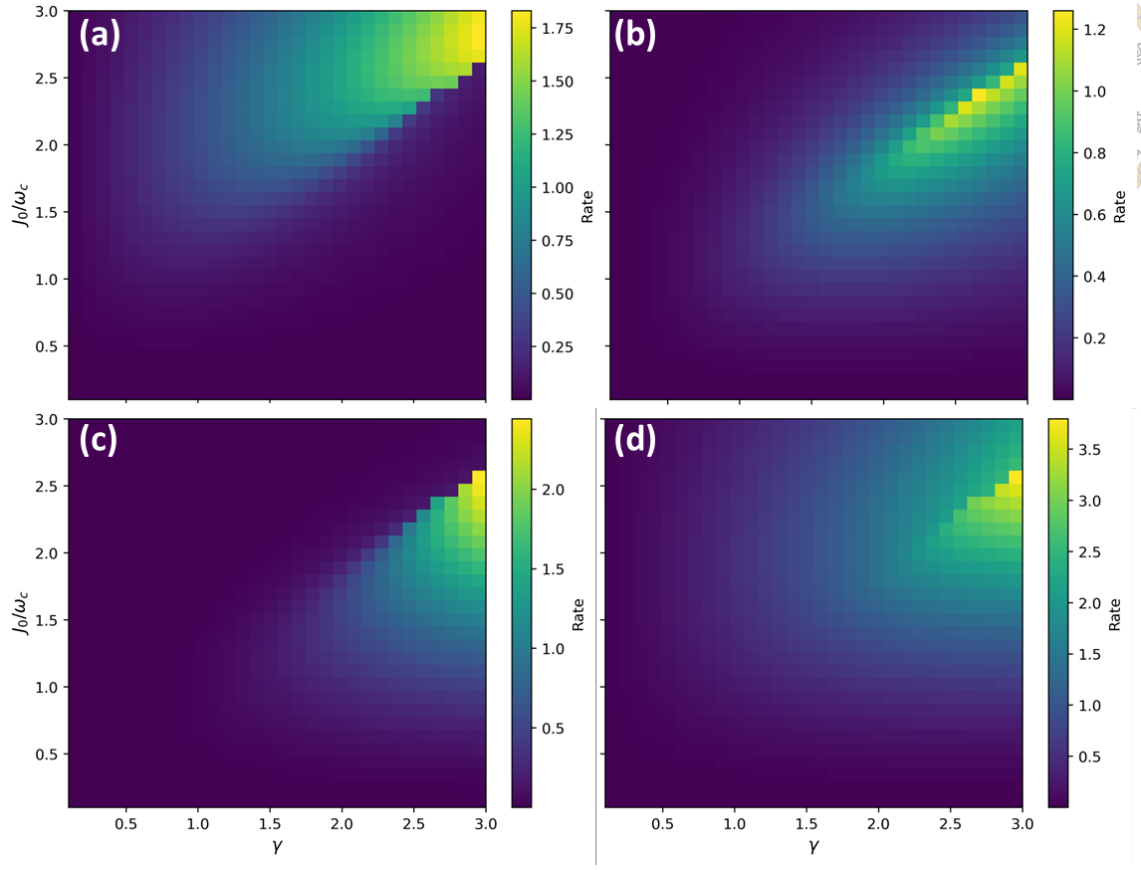

Figure 5.4: Different Markovian transfer rate terms in Eq.2.36 from donor to acceptor with Δ/ω_c=2, $\beta\omega_c$=1. (a) mRT term, (b) cross term, (c) FT term, (d) total rate.

Δ/ω_c system with $\beta\omega_c$=1. In such a large Δ/ω_c system, Fig.5.4(a) clearly shows that the mRT term dominates in a delocalized regime as well as FT term dominate in a localized regime in Fig.5.4(c) and the dividing line between the two areas is obviously consistent with the dividing line of the mixing angle ratio in Fig.5.1. Moreover, Fig.5.4(b) highlights the dominance of the cross term in an intermediate regime. Thus, in such a transitional parameter regime, traditional methods are not sufficient to describe the dynamics well.

doi:10.6342/NTU202404389

Chapter 6 Detailed Balance in the PDVPRS-QME

6.1 Detailed Balance Problem for FT and PDVPRS-QME

In this section, we will discuss the complicated detailed balance problem for FT. Owing to the perturbation, which is J_0/ω_c, FT does not work for large J_0/ω_c and small γ or large $\beta\omega_c$. Figure6.1 shows the dynamics in localized system at low temperature, evaluated by different theories in different γ. FT does not capture the correct detailed balance at the low temperature and the deviation becomes larger when γ is larger. However, PDVPRS-QME provides similar results to CMRT which are greatly better than FT. Moreover, Figure6.2 shows the dynamics evaluated by different theories in different temperature. For FT, it is clear that when temperature becomes lower, the deviation of equilibrium from QUAPI is larger. Moreover, for Fig,6.3, FT shows the same trend of deviation of detailed balance. Nevertheless, CMRT does not exhibit serious detailed balance problem in these cases.

However, for PDVPRS-QME, the detailed balance seems to depend on the mixing angle ratio ϕ. The cases of largest deviation from equilibrium in QUAPI are shown in Fig.6.2(b) where $\phi = 0.48$, and Fig.6.3(a) where $\phi = 0.23$. In contrast, CMRT and FT do

doi:10.6342/NTU202404389

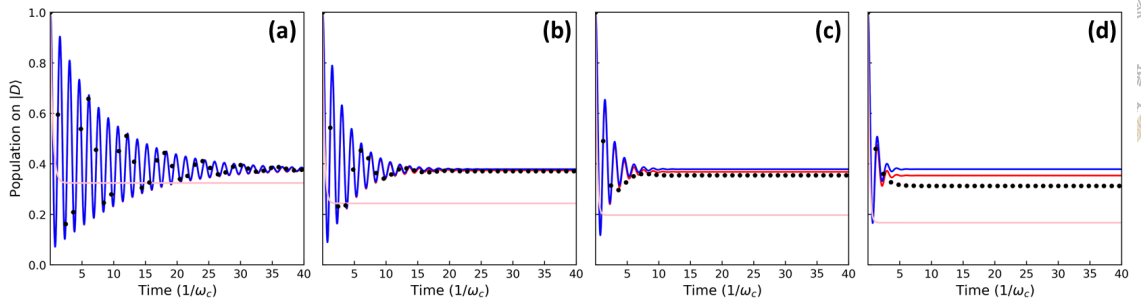

Figure 6.1: Population dynamics calculated with PDVPRS-QME (red line), CMRT (blue line), FT (pink line), QUAPI (dots) in a a small Δ/ω_c regime with different γ (a) γ=0.2, (b) γ=0.5, (c) γ=1 and (d) γ=2. Other parameters are Δ/ω_c=0.5, J_0/ω_c=1 and $\beta\omega_c = 2$.

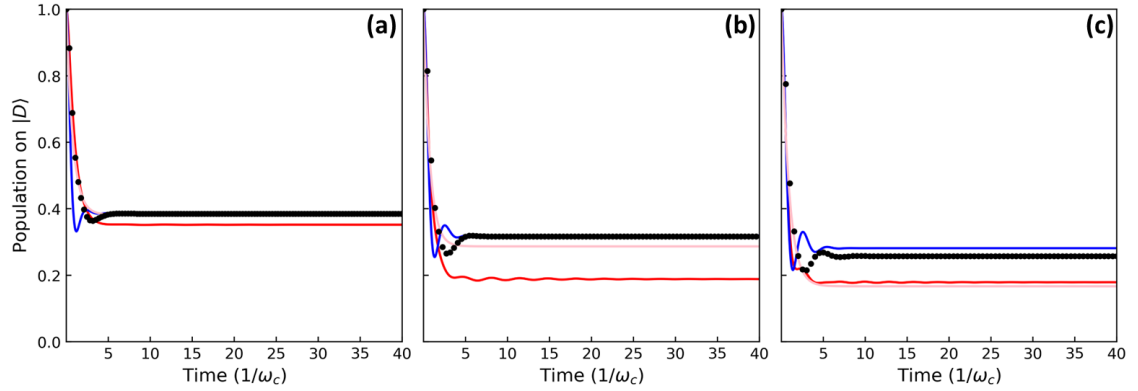

Figure 6.2: Population dynamics calculated with PDVPRS-QME (red line), CMRT (blue line), FT (pink line), QUAPI (dots) in a a small Δ/ω_c regime with different $\beta\omega_c$, (a) $\beta\omega_c$=0.5, (b) $\beta\omega_c$=1 and (c) $\beta\omega_c$=2. Other parameters are Δ/ω_c=0.5, J_0/ω_c=1 and $\gamma = 2$.

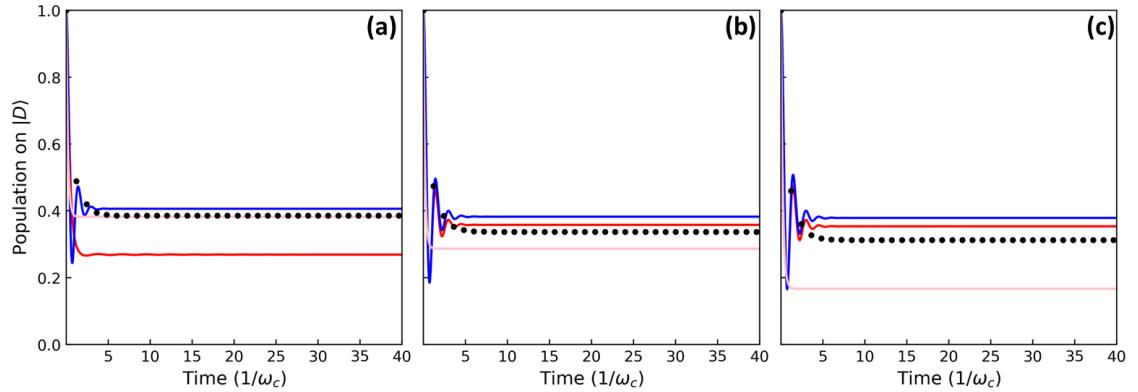

Figure 6.3: Population dynamics calculated with PDVPRS-QME (red line), CMRT (blue line), FT (pink line), QUAPI (dots) in a a small Δ/ω_c regime with different $\beta\omega_c$, (a) $\beta\omega_c$=0.5, (b) $\beta\omega_c$=1 and (c) $\beta\omega_c$=2. Other parameters are Δ/ω_c=0.5, J_0/ω_c=2 and $\gamma = 2$.

doi:10.6342/NTU202404389

not show an obvious detailed balance problem. In cases where CMRT and FT maintain correct detailed balance, PDVPRS-QME provides incorrect detailed balance if PDVPRS is in an intermediate basis, i.e., when ϕ is not close to 0 or 1.

6.2 Detailed balance problem for CMRT and FT

Finally, we present a case where CMRT and FT fail to estimate detailed balances. In Fig.6.4, both J_0/ω_c and γ, which correspond to the perturbation parameters of CMRT and FT, are large, and these two approaches do not provide correct detailed balance. However, PDVPRS-QME yields excellent results using an intermediate basis, especially in panel (c). We find that in cases where CMRT and FT fail to achieve detailed balance, PDVPRS-QME can attain accurate detailed balance through an appropriately chosen intermediate reference basis.

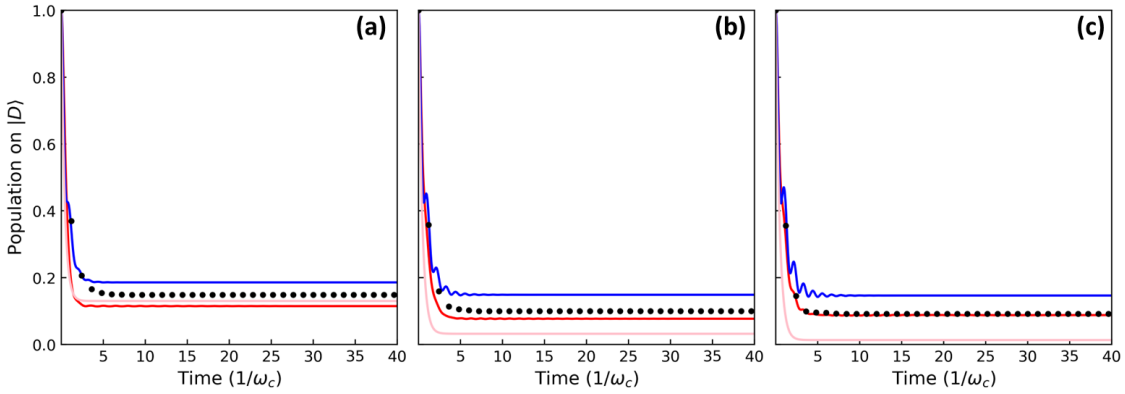

Figure 6.4: Population dynamics calculated with PDVPRS-QME (red line), CMRT (blue line), FT (pink line), QUAPI (dots) in a a small Δ/ω_c regime with different $\beta\omega_c$, (a) $\beta\omega_c$=0.5, (b) $\beta\omega_c$=1 and (c) $\beta\omega_c$=2. Other parameters are Δ/ω_c=2, J_0/ω_c=2 and $\gamma = 2$.

doi:10.6342/NTU202404389

doi:10.6342/NTU202404389

Chapter 7 Conclusion

We develop a PDVPRS-QME to effectively describe the dynamics of a electronic system in a boson bath. Deriving from a general pure dephasing reference system, we obtain a generalized pure dephasing reference system quantum master equation defined by a mixing angle θ. This QME describes not only the population transfer but also the dynamics of coherence. Moreover, diverging from conventional CMRT or FT, our method is characterized by an unique cross term in the transfer rate which is inherent from the mix perturbation. Furthermore, we utilize a variational polaron approach with the Bogoliubov' s theorem to determine the PDRS. By doing so, we identify an appropriate reference system to describe the dynamics and treats the dynamical localization effect properly.

We show the behavior of PDVPRS and benchmark PDVPRS-QME against QUAPI, CMRT and FT in a broad parameter regimes. The incorporation of variational polaron reference system allows PDVPRS to exhibit a complex behavior depending on the dynamical localization effect in temperature and system-bath coupling strengths. Moreover, PDVPRS-QME exhibits broadened applicability across different regimes, avoiding limitations in traditional theories. However, PDVPRS-QME has a problem of abrupt transition of mixing angle which is an artifact of the variational small poloronic ansatz. We can improve this issue via a more sophisticated variational polaron approach in the future work. Furthermore, we highlight the importance of cross term in an intermediate regime between

doi:10.6342/NTU202404389

the Redfield picture and Förster picture. However, the problem of detailed balance still an issue to be resolve. For other spectral density like Ohmic and Drude—Lorentz types, the divergence of integral is a problem to the small polaron approach.

Finally, we believe the general concept of the PDVPRS-QME approach developed in this work can be extended beyond a dimer to larger systems and applied to more general quantum dynamics problems, such as electron transfer or charge mobility in complex systems, providing a novel perspective for deriving QME.

doi:10.6342/NTU202404389

References

[1] Gregory D Scholes and Garry Rumbles. Excitons in nanoscale systems. *Nat. Mater.*, 5:683–696, 2006.

[2] Richard John Cogdell, Alastair Thomas Gardiner, Hideki Hashimoto, and Tatas Hardo Panintingjati Brotosudarmo. A comparative look at the first few milliseconds of the light reactions of photosynthesis. *Photochem. Photobiol. Sci.*, 7:1150–1158, 2008.

[3] Yuan-Chung Cheng and Graham R Fleming. Dynamics of light harvesting in photosynthesis. *Annu. Rev. Phys. Chem.*, 60:241–262, 2009.

[4] Gregory D Scholes, Graham R Fleming, Alexandra Olaya-Castro, and Rienk Van Grondelle. Lessons from nature about solar light harvesting. *Nat. Chem.*, 3:763–774, 2011.

[5] Neill Lambert, Yueh-Nan Chen, Yuan-Chung Cheng, Che-Ming Li, Guang-Yin Chen, and Franco Nori. Quantum biology. *Nat. Phys.*, 9:10–18, 2013.

[6] Th Förster. Zwischenmolekulare energiewanderung und fluoreszenz. *Ann. Phys.*, 437:55–75, 1948.

[7] Hitoshi Sumi. Theory on rates of excitation-energy transfer between molecular ag-

doi:10.6342/NTU202404389

gregates through distributed transition dipoles with application to the antenna system in bacterial photosynthesis. *J. Phys. Chem. B*, 103:252–260, 1999.

[8] Seogjoo Jang, Marshall D Newton, and Robert J Silbey. Multichromophoric Förster resonance energy transfer. *Phys. Rev. Lett.*, 92:218301, 2004.

[9] Wei Min Zhang, Torsten Meier, Vladimir Chernyak, and Shaul Mukamel. Exciton-migration and three-pulse femtosecond optical spectroscopies of photosynthetic antenna complexes. *J. Chem. Phys.*, 108:7763–7774, 1998.

[10] Mino Yang and Graham R Fleming. Influence of phonons on exciton transfer dynamics: comparison of the Redfield, Förster, and modified Redfield equations. *Chem. Phys.*, 282:163–180, 2002.

[11] Yu Chang and Yuan-Chung Cheng. On the accuracy of coherent modified Redfield theory in simulating excitation energy transfer dynamics. *J. Chem. Phys.*, 142, 2015.

[12] Y. Chang and Y. C. Cheng. On the accuracy of coherent modified Redfield theory in simulating excitation energy transfer dynamics. *J. Chem. Phys.*, 142, 2015.

[13] Anton Trushechkin. Calculation of coherences in Förster and modified Redfield theories of excitation energy transfer. *J. Chem. Phys.*, 151, 2019.

[14] Vladimir Novoderezhkin, Alessandro Marin, and Rienk van Grondelle. Intra- and inter-monomeric transfers in the light harvesting lhcii complex: the Redfield–Förster picture. *Phys. Chem. Chem. Phys.*, 13:17093–17103, 2011.

[15] Vladimir Novoderezhkin and Rienk van Grondelle. Spectra and dynamics in the b800 antenna: Comparing hierarchical equations, Redfield and Förster theories. *J. Phys. Chem. B*, 117:11076–11090, 2013.

doi:10.6342/NTU202404389

[16] Vladimir I Novoderezhkin and Rienk Van Grondelle. Modeling of excitation dynamics in photosynthetic light-harvesting complexes: exact versus perturbative approaches. *J. Phys. B: At. Mol. Opt. Phys.*, 50:124003, 2017.

[17] Thomas Renger, Mohamed E Madjet, A Knorr, and Frank Müh. How the molecular structure determines the flow of excitation energy in plant light-harvesting complex ii. *J. Plant Physiol.*, 168:1497–1509, 2011.

[18] Thanh Nhut Do, Hoang Long Nguyen, Parveen Akhtar, Kai Zhong, Thomas LC Jansen, Jasper Knoester, Stefano Caffarri, Petar H Lambrev, and Howe-Siang Tan. Ultrafast excitation energy transfer dynamics in the lhcii–cp29–cp24 subdomain of plant photosystem ii. *J. Phys. Chem. Lett.*, 13:4263–4271, 2022.

[19] Andrei A Golosov and David R Reichman. Reference system master equation approaches to condensed phase charge transfer processes. i. general formulation. *J. Chem. Phys.*, 115:9848–9861, 2001.

[20] Andrei A Golosov and David R Reichman. Reference system master equation approaches to condensed phase charge transfer processes. ii. numerical tests and applications to the study of photoinduced charge transfer reactions. *J. Chem. Phys.*, 115:9862–9870, 2001.

[21] Yuan-Chung Cheng and Robert J Silbey. A unified theory for charge-carrier transport in organic crystals. *J. Chem. Phys.*, 128, 2008.

[22] Hung-Tzu Chang and Yuan-Chung Cheng. Coherent versus incoherent excitation energy transfer in molecular systems. *J. Chem. Phys.*, 137, 2012.

[23] Hung-Tzu Chang, Pan-Pan Zhang, and Yuan-Chung Cheng. Criteria for the accuracy

doi:10.6342/NTU202404389

of small polaron quantum master equation in simulating excitation energy transfer dynamics. *J. Chem. Phys.*, 139, 2013.

[24] Hung-Hsuan Teh, Bih-Yaw Jin, and Yuan-Chung Cheng. Frozen-mode small polaron quantum master equation with variational bound for excitation energy transfer in molecular aggregates. *J. Chem. Phys.*, 150, 2019.

[25] Seogjoo J Jang. Partially polaron-transformed quantum master equation for exciton and charge transport dynamics. *J. Chem. Phys.*, 157, 2022.

[26] JL Skinner and D Hsu. Pure dephasing of a two-level system. *J. Phys. Chem.*, 90:4931–4938, 1986.

[27] David W Brown, Katja Lindenberg, and Yang Zhao. Variational energy band theory for polarons: Mapping polaron structure with the global-local method. *J. Chem. Phys.*, 107:3179–3195, 1997.

[28] Vladimir I Novoderezhkin and Rienk van Grondelle. Physical origins and models of energy transfer in photosynthetic light-harvesting. *Phys. Chem. Chem. Phys.*, 12:7352–7365, 2010.

doi:10.6342/NTU202404389